Chaos

Phase-field-crystal description of active crystallites: Elastic and inelastic collisions

Lukas Ophaus, Johannes Kirchner, (iD) Svetlana V. Gurevich, and (iD) Uwe Thiele
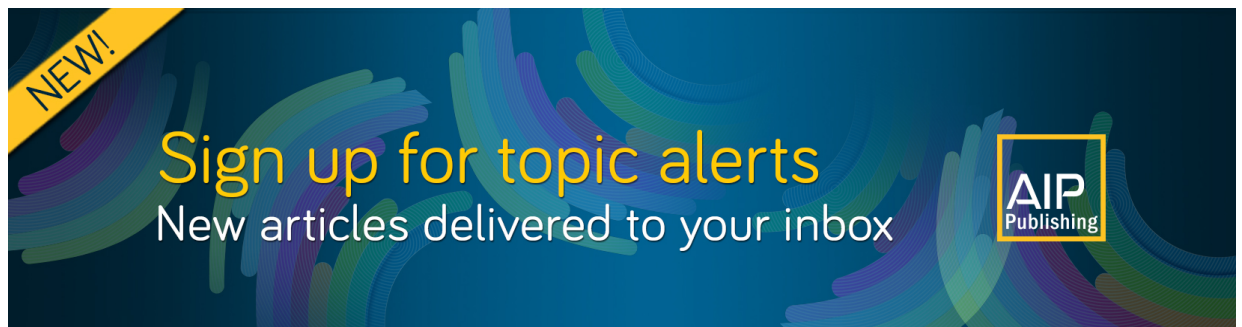
View Online   Export Citation   CrossMark

Phase-field-crystal description of active crystallites: Elastic and inelastic collisions

Lukas Ophaus,[1,2] Johannes Kirchner,[1] Svetlana V. Gurevich,[1,2] and Uwe Thiele[1,2,a]

AFFILIATIONS

[1] Institut für Theoretische Physik, Westfälische Wilhelms-Universität Münster, Wilhelm-Klemm-Strasse 9,
48149 Münster, Germany
[2] Center of Nonlinear Science (CeNoS), Westfälische Wilhelms-Universität Münster, Corrensstrasse 2, 48149 Münster, Germany

[a] **Author to whom correspondence should be addressed:** u.thiele@uni-muenster.de. **URL:** http://www.uwethiele.de

ABSTRACT

The active Phase-Field-Crystal (aPFC) model combines elements of the Toner–Tu theory for self-propelled particles and the classical Phase-Field-Crystal (PFC) model that describes the transition between liquid and crystalline phases. In the liquid-crystal coexistence region of the PFC model, crystalline clusters exist in the form of localized states that coexist with a homogeneous background. At sufficiently strong activity (related to self-propulsion strength), they start to travel. We employ numerical path continuation and direct time simulations to first investigate the existence regions of different types of localized states in one spatial dimension. The results are summarized in morphological phase diagrams in the parameter plane spanned by activity and mean density. Then we focus on the interaction of traveling localized states, studying their collision behavior. As a result, we distinguish "elastic" and "inelastic" collisions. In the former, localized states recover their properties after a collision, while in the latter, they may completely or partially annihilate, forming resting bound states or various traveling states.

Published under license by AIP Publishing. https://doi.org/10.1063/5.0019426

We employ numerical path continuation and direct time simulations to investigate the existence regions and interaction of traveling localized crystalline patches, i.e., traveling localized states, in a one-dimensional active Phase-Field-Crystal (aPFC) model. The aPFC system describes transitions between a liquid phase and resting and traveling crystalline phases of ensembles of active particles. Based on an extensive bifurcation analysis of the parameter regions where the various localized states exist, we focus on an exploration of their collision behavior. It ranges from one-to-one collisions to interactions of ensembles of localized states. This analysis allows us to distinguish "elastic" and "inelastic" collisions and to introduce concepts as the critical free path necessary for fully elastic collisions.

I. INTRODUCTION

The formation of patterns has always been an intriguing phenomenon for scientists and laypersons alike. Regular spatial, temporal, and spatiotemporal patterns universally occur in nature ranging from physical, chemical, and biological systems to geological and even social systems.[1–4] Classifying macroscopic physical systems, one can distinguish, on the one hand, passive systems that are normally closed and develop toward thermodynamic equilibrium. The resulting structures can show spatial patterns like, e.g., regular crystal lattices, and one normally relates them to self-assembly as typical structure lengths directly result from the properties of individual constituents. On the other hand, there are active or out-of equilibrium systems that are usually open systems and develop under permanent energy conversion. They normally show self-organized and dissipative structures whose typical length scales depend on transport coefficients and rate constants.[5] Such structures do not persist when the driving fluxes are switched off. One example are systems composed of active particles[6–9] that transform, e.g., chemical into mechanical energy, resulting in their self-propelled directed motion.[10,11] Ensembles of such particles can show fascinating collective phenomena. Long- and short-range interactions between the particles can result in polar ordering and a synchronization of the particle motion.[12,13] The coordinated collective motion of many such active particles is often called swarming.[10] Striking examples are schools of fish and flocks of birds, sometimes referred to as "living particles." Besides the naturally occurring examples of self-propelled

organisms, artificial active particles are also developed. For instance, there exist micro-swimmers that employ light,[14,15] ultrasound,[16,17] or chemical energy[18] to fuel their "engines."

Similar to the case of equilibrium systems, for the active particles, one can distinguish different phases of the ensemble behavior. Parameters like the particle density, the strength of the active driving of individual particles, and the strength and specific type of interactions between neighboring particles determine whether one encounters motility-induced clustering or random motion of individual particles or moving swarms with a high degree of spatial order. Such ordered swarms may be seen as a crystalline state, while the disordered states may be seen as gas-like or liquid-like.[11,19] Phase separation between such gas- and liquid-like states can be induced by solely changing the particle motility.[20–22] At very high densities, highly ordered resting[23,24] and traveling[11,14,25–29] crystalline states can also be formed. A distinction between gas-like or liquid-like ensemble behavior is also made for localized spots observed in gas-discharge systems and liquid crystal light-valve experiments.[30–32]

Systems of active particles are often investigated with particle-based models employing large-scale direct numerical simulations. Besides, there exists a wide range of continuum models for active media.[10,28,33,34] For instance, the Toner–Tu model is a prominent continuum theory for "flocking"[35,36] that expands the Navier–Stokes description of classical fluids by various active terms that break the Galilean invariance by distinguishing the frame of reference of resting particles. Elements of the Toner–Tu model are combined with the Phase-Field-Crystal (PFC) model to form a simple model for active interacting particles.[37] The PFC model is widely employed as a generic continuum model to study the dynamics of atomistic and colloidal crystallization on microscopic length and diffusive time scales.[38–41] In the context of continuum models for pattern formation,[5] the PFC model represents an equivalent of the Swift–Hohenberg (SH) equation with mass-conserving dynamics. The SH equation is a generic equation for the formation of steady patterns close to a small-scale instability and does not conserve mass. Therefore, the PFC model is sometimes called the conserved Swift–Hohenberg (cSH) equation.[42,43]

The resulting active Phase-Field-Crystal model (aPFC)[37] describes transitions between a liquid phase and resting and traveling crystalline phases of ensembles of active particles.[37,44–46] On the technical level, the aPFC model couples the passive cSH equation that describes the dynamics of a density-like conserved order parameter field with the nonconserved dynamics of a polarization field that represents the coarse-grained orientation and direction of motion of the self-propelled particles. Employing the aPFC model, a variety of periodic[37,45] and localized[46] active crystals is described in the literature. The additional influence of hydrodynamic interactions is also studied[44] by incorporating an additional velocity field into the model.

The main subject of the present work is the existence and interaction of active crystallites, i.e., localized crystalline patches, also known as localized states of the aPFC equation. In general, localized states are experimentally observed and modeled in various areas of biology, chemistry, and physics.[31,47–53] Examples include localized spots in reaction–diffusion systems,[51] localized patches of vegetation patterns in a bare background,[54,55] local arrangements of free-surface spikes of magnetic fluids occurring in the bistable region

just below the onset of the Rosensweig instability,[56] localized spot patterns in nonlinear optical[57] and gas-discharge[30] systems, traveling wave pulses in binary convection,[58,59] and oscillating localized states (oscillons) in vibrated layers of colloidal suspensions.[60]

In the context of solidification described by PFC models, localized states are observed in and near the thermodynamic coexistence region of liquid and crystal states. Crystalline patches of various size and symmetry can coexist with a liquid environment depending on control parameters such as mean density and temperature.[42,61,62] For instance, increasing the mean density, the crystallites increase in size as further density peaks (depending on context also called "bumps" or "spots") are added at the crystal–liquid interface. Ultimately, the whole domain fills up and for a finite domain, branches of localized states in a bifurcation diagram terminate on a branch of space filling periodic states. Within their existence region, branches of different localized states form a typical slanted snakes-and-ladders structure corresponding to homoclinic snaking.[63,64] The slant is an important property resulting from the presence of a conservation law in the PFC model.[42,43,65–68] In contrast, without conservation law, e.g., in the case of the SH model, the snaking curves of localized states are aligned.[63,69,70] The relation between slanted and aligned snaking in closely related systems with and without conservation law, respectively, is discussed in Refs. 42 and 62.

A first investigation of localized states in an active PFC model is given in Ref. 46 that determines the linear stability of homogeneous states, analyzes the onset of motion of periodic and localized states in one-dimensional domains and provides corresponding bifurcation diagrams. The present work first deepens this analysis by providing a more extensive analysis of the parameter regions where the various localized states exist. Selected bifurcation diagrams are combined with "existence diagrams" showing where the various states occur. The knowledge gained is then combined with morphological phase diagrams obtained by direct time simulation. This forms the basis of an exploration of the collision behavior of localized states ranging from one-to-one collisions of traveling localized states to interactions of several localized states. This allows us to introduce concepts such as the critical free path necessary for fully elastic collisions.

Our work is structured as follows: in Sec. II, we briefly present the active PFC model and discuss its analytical and numerical treatment. After reviewing the linear stability of the liquid phase and the overall phase behavior in Sec. III, spatially localized states are discussed in Sec. IV with additional material given in the Appendix. Their bifurcation structure is analyzed focusing on the two main control parameters, mean density and activity. The analysis of the collision behavior is presented in Sec. V. The final Sec. VI provides a conclusion and outlook.

II. THE MODEL

A. Governing equations

The active PFC model is introduced by Menzel and Löwen in Ref. 37. Its order parameters are the nondimensional scalar field $\psi(\mathbf{r}, t)$ that corresponds to a scaled shifted density and the nondimensional vector field $\mathbf{P}(\mathbf{r}, t)$, referred to as "polarization." It denotes the local coarse grained orientational order of the active

particles that is identical to the net direction of self-propulsion. In particular, $\psi(\mathbf{r}, t)$ is the modulation about a fixed reference density $\overline{\psi}$, hence $\int_{\Omega} \psi \, d^n r = 0$, where $\mathbf{r} \in \Omega \subset \mathbb{R}^n$ and Ω is the considered domain in n-dimensional space. As $\overline{\psi}$ controls the amount of material in the system, in the following, it is referred to as mean density and is employed as one main control parameter.

The nondimensional aPFC model[37] combines a conserved dynamics for the density

$$\partial_t \psi = \nabla^2 \frac{\delta \mathscr{F}}{\delta \psi} - \upsilon_0 \nabla \cdot \mathbf{P}, \qquad (1)$$

and a nonconserved dynamics of the polarization field

$$\partial_t \mathbf{P} = \nabla^2 \frac{\delta \mathscr{F}}{\delta \mathbf{P}} - D_r \frac{\delta \mathscr{F}}{\delta \mathbf{P}} - \upsilon_0 \nabla \psi. \qquad (2)$$

Here, the activity υ_0 corresponds to the strength of self-propulsion and is at the same time the strength of the only coupling of the fields. In the following, we refer to it as "activity." The employed coupling is linear and has the simplest allowed form that does not break the conservation of ψ,[37,45,46] i.e., its evolution still follows a continuity equation $\partial_t \psi = -\nabla \cdot \mathbf{j}$ with a flux $\mathbf{j}$. For a derivation of the model from a corresponding Dynamical Density Functional Theory (DDFT) for active colloidal particles, see Ref. 44.

The polarization $\mathbf{P}$ represents the strength and direction of local polar ordering. The translational and rotational diffusion of the particles in the DDFT give rise to the conserved first and non-conserved second term in Eq. (2), respectively, where D_r is the diffusional mobility of rotational diffusion. A source term for the polarization is proportional to the density gradient. Note that advection with the material flux $\mathbf{j}$ is not considered, i.e., it is assumed that diffusive processes dominate the polarization dynamics.

In the limiting case of a passive system ($\upsilon_0 = 0$), the dynamics of $\psi(\mathbf{r}, t)$ and $\mathbf{P}(\mathbf{r}, t)$ is variational, i.e., the two equations reduce to a respective gradient dynamics on the underlying free energy functional $\mathscr{F}[\psi, \mathbf{P}]$. If the functional does not contain any energetic coupling (as is the case here), the dynamics of ψ and $\mathbf{P}$ completely decouple. The free energy functional

$$\mathscr{F} = \mathscr{F}_{\mathrm{pfc}} + \mathscr{F}_{\mathbf{P}} \qquad (3)$$

is composed of the standard Phase-Field-Crystal functional[38,39,71] (identical to the Swift–Hohenberg functional[5])

$$\mathscr{F}_{\mathrm{pfc}}[\psi] = \int d^n r \left\{ \frac{1}{2} \psi \left[\epsilon + \left(1 + \nabla^2\right)^2 \right] \psi + \frac{1}{4} (\psi + \overline{\psi})^4 \right\}, \qquad (4)$$

and the orientational part

$$\mathscr{F}_{\mathbf{P}}[\mathbf{P}] = \int d^n r \left(\frac{C_1}{2} |\mathbf{P}|^2 + \frac{C_2}{4} |\mathbf{P}|^4 \right). \qquad (5)$$

The functional (3) describes transitions between a uniform and a periodically patterned state.[39] The negative interfacial energy density ($\sim -|\nabla \psi|^2$, obtained by partial integration from the $\psi \nabla^2 \psi$ term), favors the creation of interfaces and is limited only by the stiffness term ($\sim (\nabla^2 \psi)^2$). The quartic bulk energy contains the temperature-like parameter ϵ. For negative values (low temperatures, i.e., for an undercooled liquid), a periodic (crystalline) state forms, while high temperatures result in a uniform (liquid) phase.

The orientational part [Eq. (5)] with $C_1 < 0$ and $C_2 > 0$ represents a double-well potential that results in a spontaneous polarization of absolute value $\sqrt{-C_1/C_2}$ and arbitrary orientation. Here, we concentrate on the already rich behavior obtained for positive $C_1 > 0$ and vanishing $C_2 = 0$, as our analysis shall directly connect to former studies.[37,44–46] At positive $C_1 > 0$, diffusion tends to reduce the polarization.

Introducing the functional (3) into Eqs. (1) and (2) and executing the variations yields the coupled evolution equations

$$\partial_t \psi = \nabla^2 \left\{ \left[\epsilon + \left(1 + \nabla^2\right)^2 \right] \psi + \left(\overline{\psi} + \psi\right)^3 \right\} - \upsilon_0 \nabla \cdot \mathbf{P}, \quad (6)$$

$$\partial_t \mathbf{P} = C_1 \nabla^2 \mathbf{P} - D_r C_1 \mathbf{P} - \upsilon_0 \nabla \psi, \qquad (7)$$

where the equation for $\mathbf{P}$ is fully linear. Note that the equations are invariant under the reflection $\kappa : (\mathbf{r}, \psi, \mathbf{P}) \to (-\mathbf{r}, \psi, -\mathbf{P})$. This κ-symmetry takes the role of parity for the present model that couples a scalar field and a vector field. Below, we refer to κ-symmetric (-asymmetric) states as symmetric (asymmetric) states.

B. Steady and stationary states

In the following, we study Eqs. (6) and (7) in one spatial dimension (1D). Then, the polarization becomes a scalar field $P(x, t)$ that describes the coarse grained strength of local ordering and self-propulsion as well as its sense of direction. Besides fully time-dependent behavior studied by direct numerical simulation, we analyze stable and unstable steady and stationary states of the system. Here, we denote states at rest as "steady," while uniformly traveling states are denoted as "stationary." The latter are steady in a frame moving with some constant velocity c. After a coordinate transformation into the comoving frame, i.e., replacing $\partial_t \psi = c \partial_x \psi$ and $\partial_t P = c \partial_x P$, we integrate Eq. (6) once and obtain the system of ordinary differential equations (ODEs)

$$0 = \partial_x \left\{ \left[\epsilon + (1 + \partial_{xx})^2 \right] \psi + \left(\overline{\psi} + \psi\right)^3 \right\} - \upsilon_0 P - c\psi - j, \quad (8)$$

$$0 = C_1 \partial_{xx} P - D_r C_1 P - \upsilon_0 \partial_x \psi - c \partial_x P. \qquad (9)$$

Here, the integration constant j represents the constant flux in the comoving frame. For resting states, velocity c and flux j are zero, while for traveling states they have to be determined together with the solution profiles. Note that in 1D, the field P corresponds to a pseudo-scalar and the κ-symmetry becomes $\kappa : (x, \psi, P) \to (-x, \psi, -P)$.

The trivial liquid (uniform) state ($\psi_0 = 0, P_0 = 0$) always solves Eqs. (8) and (9). Its linear stability is discussed in Sec. III. Changes in stability of the liquid state are related to bifurcations where resting and traveling crystalline (periodic) states emerge and these, in turn, give rise to branches of crystallites (localized states) in secondary bifurcations. Bifurcation diagrams show how the various branches of such spatially modulated states [$\psi = \psi(x)$, $P = P(x)$] are related. To determine them, we transform Eqs. (8) and (9) into a system of seven first order ODEs, employ periodic boundary conditions, an integral condition for mass conservation and an integral condition that projects out the translational symmetry mode, and employ the numerical pseudo-arclength continuation

techniques[62,72,73] bundled in the toolbox AUTO07P.[74,75] For detailed explanations and hands-on tutorials, see Refs. 62 and 76. In the context of SH and PFC (cSH) models, such methods are extensively used, e.g., in Refs. 42, 52, 69, and 77. However, they are less frequently applied to the aPFC model[46] and other models of active matter.[78,79]

For the direct numerical simulation, we use a pseudo-spectral method. After choosing initial conditions, Eqs. (6) and (7) are integrated forward in time via a semi-implicit Euler method, while spatial derivatives and nonlinearities are calculated in Fourier space and in real space, respectively.

III. OVERALL PHASE BEHAVIOR

As mentioned above, the trivial uniform liquid state $(\psi_0, P_0) = (0, 0)$ solves Eqs. (8) and (9) for any mean density $\overline{\psi}$ and activity v_0. However, it may be linearly stable or unstable as can be deduced by a linear stability analysis, i.e., by a linearization of Eqs. (6) and (7) in small fluctuations about the uniform state. This is done in Ref. 46 where the resulting dispersion relations are discussed in detail (also cf. Refs. 37 and 45). On the one hand, the uniform state can be unstable to a stationary small-scale (Turing) instability. For the uncoupled (passive) system $(v_0 = 0)$, the critical wavenumber is $q_{crit} = 1$. In the coupled (active) case $(v_0 \neq 0)$, the critical wavenumber slightly differs from $q_{crit} = 1$. In this case, the eigenvalue is real-valued at instability-filling onset, the primary bifurcation is a pitchfork bifurcation, and the emerging nonlinear periodic state corresponds to a resting crystal (red line and dark gray shaded region in Fig. 1). On the other hand, the uniform state can be unstable to an oscillatory small-scale

FIG. 1. Linear stability and morphological phase diagram indicating where in the parameter plane spanned by activity v_0 and mean density $\overline{\psi}$ the three basic domain-filling states can occur based on linear stability considerations. Namely, these are the liquid (uniform) and the resting and traveling crystalline (periodic) states. The red line separates the liquid state (no shading) and the resting crystalline state (dark gray shaded), whereas the blue line separates the liquid state and the traveling crystalline state (yellow shaded). The vertical dashed line at $v_0 \approx 0.158$ indicates the transition between resting and traveling crystal. The remaining parameters are $\epsilon = -1.5$, $D_r = 0.5$, $C_1 = 0.1$, and $C_2 = 0$.

instability. There, the eigenvalue at onset is complex-valued, the primary bifurcation is a Hopf bifurcation, and the emerging state is a traveling crystal (blue line and yellow shaded region in Fig. 1). Note that, for simplicity, the corresponding instability thresholds (solid lines in Fig. 1) are determined at imposed $q_{crit} = 1$. On the scale of Fig. 1, the result cannot be distinguished from the exact one.

Above onset, the boundary between resting and traveling crystals cannot be determined by a linear analysis of the uniform state. However, it can be obtained employing a velocity expansion close to the drift-pitchfork bifurcation responsible for the transition.[46] The resulting condition for the onset of motion of all types of steady states is
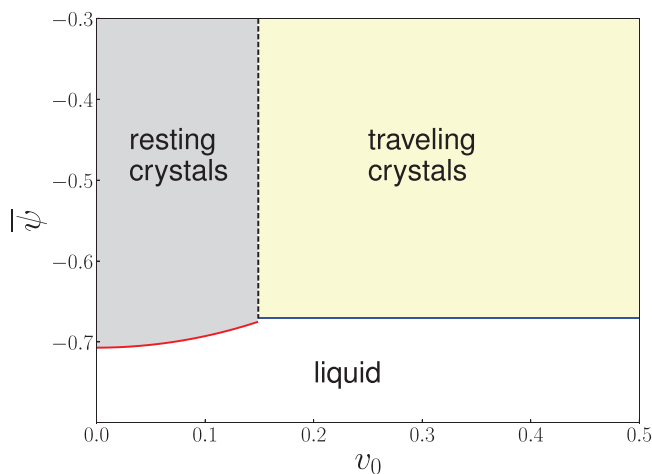
$$\|\psi\|_2 - \|P\|_2 = 0. \tag{10}$$

Here, $\|\psi\|_2$ and $\|P\|_2$ are the L^2-norms of the density and polarization field of the resting state, respectively. It is remarkable that the critical activity ($v_0^c \approx 0.15$ in Fig. 1) is virtually independent of mean density. This is similar to the results of Ref. 45 on the dependence of this boundary on an effective temperature.

The corresponding boundary (vertical dashed line in Fig. 1) is obtained by tracking the condition (10) while numerically continuing the fully nonlinear states. Practically, Eq. (10) is used as additional integral condition allowing one to directly track the onset of motion in the $(v_0, \overline{\psi})$-plane. The continuation result perfectly agrees with the onset of motion obtained by direct time simulations.[46] Note that due to periodic boundary conditions and fixed domain size, the traveling crystal keeps its spatial periodicity. We emphasize that criterion (10) is valid for any steady state and is used in Sec. IV to detect different types of drift bifurcations of various localized states. The corresponding critical values of v_0 are very close but not identical to the one for periodic states.

IV. LOCALIZED STATES

Similar to the passive PFC model,[42] the active PFC model exhibits a wide range of different localized states (LS).[46] These are finite patches of a periodic structure embedded in a homogeneous background, i.e., finite size crystals in coexistence with the liquid phase. For a discussion how these LS are related to the liquid-crystal phase transition in the thermodynamic limit, i.e., how the Maxwell construction emerges when the domain size is increased toward infinity, see Ref. 77. Here, we refer to the LS as crystallites. In contrast to the passive PFC model, where all states are at rest, for the active PFC model, resting and uniformly traveling crystallites are described,[46] with a transition at finite critical values of the activity v_0. The onset of motion occurs at finite critical values of the activity v_0 through a drift-pitchfork or a drift-transcritical bifurcation. It can be predicted using criterion (10). Selected first bifurcation diagrams for LS are given in Ref. 46. Here, we scrutinize the emergence of resting and traveling LS in detail and determine their regions of existence. This information is subsequently used in Sec. V to study the collision behavior of traveling LS.

As in Ref. 46, we focus on activity v_0 and mean density $\overline{\psi}$ as the main control parameters. As the onset of motion is largely independent of $\overline{\psi}$ (cf. Fig. 1), we base our analysis on bifurcation diagrams with control parameter v_0 obtained at different fixed $\overline{\psi}$. We begin with the passive case.

A. Slanted snaking in the passive case

For the passive PFC model, the existence of steady LS and their intricate bifurcation structure of slanted homoclinic snaking is studied for 1D[42,62,77] and 2D systems.[62,77] They are obtained by solving Eqs. (8) and (9) with $\upsilon_0 = 0$. Here, Fig. 2 presents as a reference case a corresponding bifurcation diagram employing the mean density $\overline{\psi}$ as the control parameter. The effective temperature is $\epsilon = -1.5$ and the domain size is $L = 100$ as in Ref. 42. As a solution measure, we employ the L^2-norm $||\psi||_2$ of the density profile as it is well suited to distinguish the various states. For typical corresponding plots of chemical potential, Helmholtz free energy, and grand potential, see Refs. 42 and 77.

The liquid (homogeneous) state $\psi(x) = 0$ has zero norm and is represented by $\overline{\psi}$-axis. It is stable at small densities (strongly negative $\overline{\psi}$) and is destabilized at a critical mean density of $\overline{\psi}_c \approx -0.71$ where a branch of crystalline (periodic) states bifurcates in a supercritical pitchfork bifurcation in agreement with the linear stability result for the liquid state (cf. $\upsilon_0 = 0$ in Fig. 1). For the chosen domain size, these profiles have 16 density peaks. Branches of periodic states with 15 and 17 peaks emerge at a slightly larger $\overline{\psi}$ (not
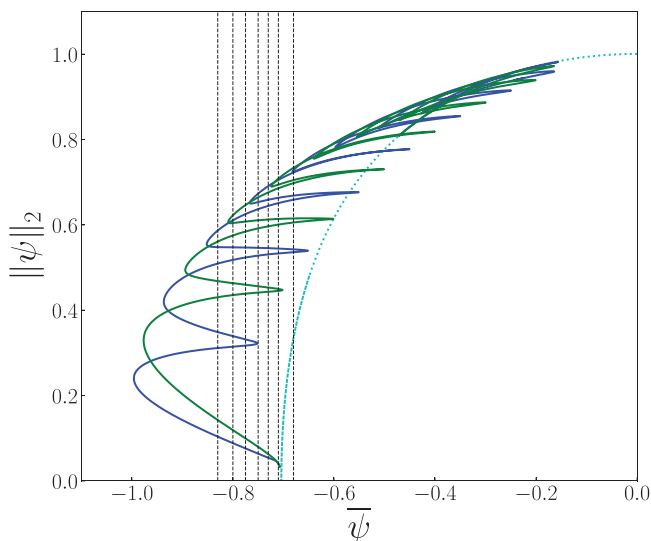
FIG. 2. Shown is an example of slanted homoclinic snaking of steady localized states for the passive PFC model, i.e., Eqs. (8) and (9) with $\upsilon_0 = 0$. The bifurcation diagram shows the norm in dependence of mean density $\overline{\psi}$. At $\overline{\psi} \approx -0.71$, a branch of crystalline (periodic) states with 16 peaks (dotted cyan line) bifurcates off the liquid state (line of zero norm) in a supercritical pitchfork bifurcation. Slightly afterward two branches of crystallites (LS) branch off subcritically from this branch of periodic states. They consist of symmetric localized steady states with an odd (blue lines) and an even (green lines) number of peaks, respectively. Undergoing a sequence of nonaligned saddle-node bifurcations, they snake toward a larger mean density and norm until ending on a branch of periodic states with 15 peaks (not shown). Here, and in the following figures, the branches of asymmetric LS are not included. The vertical dashed lines mark the particular fixed values of $\overline{\psi} = -0.83, -0.80, -0.775, -0.75, -0.73, -0.71,$ and -0.68 for which bifurcation diagrams in υ_0 are presented below. Parameters are $\epsilon = -1.5$, $D_r = 0.5$, $C_1 = 0.1$, $C_2 = 0$, and a domain size of $L = 100$.

shown). Above the $\overline{\psi}$ value where the 16-peak branch emerges, fluctuations perturbing the liquid state grow exponentially and a spatially extended crystals or LS form. The supercritical 16-peak branch itself is only stable in a very small parameter range close to the primary bifurcation. Then, in a secondary bifurcation, two subcritical branches of LS simultaneously emerge. For diverging domain size, the secondary bifurcation coincides with the primary one. The two branches consist of LS that gain stability at a first saddle-node bifurcation and then lose and gain stability "periodically" as the branches snake toward a larger $\overline{\psi}$ acquiring larger norms in the process. The two snaking branches consist of κ-symmetric LS and show an even and an odd number of density peaks, respectively. In each "period" of the snaking they symmetrically gain two peaks until the LS fill the domain and the branches end on the branch of 15-peak periodic states. Beyond this bifurcation the latter branch is stable. Further, branches of unstable steady κ-asymmetric LS exist that connect the two branches of symmetric LS. Here, they are always unstable and are, therefore, not included in the bifurcation diagrams. We characterize individual LS by the number n of density peaks they consist of, i.e., we speak of n-peak states. For more details including a discussion of the dependence of the entire bifurcation structure on effective temperature, see Ref. 42. The relation of the slanted snaking structure obtained at finite domain size and the Maxwell construction in the thermodynamic limit is discussed in Ref. 77.

Here, the slanted snaking structure of Fig. 2 serves as a starting point for an extensive investigation of active crystallites. In Sec. IV B and in the Appendix we present bifurcation diagrams in dependence of υ_0 at several fixed values of $\overline{\psi}$. They are indicated in Fig. 2 by vertical dashed lines. This shall allow us to understand how the numerous branches of traveling LS come into existence, allow for the construction of existence diagrams, and, ultimately, guide our numerical experiments on the interaction of traveling LS.

B. Crystallites in the active case

From here on, we only consider the active PFC model. Next, we determine steady and stationary states by solving Eqs. (8) and (9) for $\upsilon_0 \neq 0$. Note that the velocity c is unknown and determined as a nonlinear eigenvalue. The rich set of LS obtained in Sec. IV A for the passive case is now employed as reference at the corresponding values of $\overline{\psi}$. First, the relatively small value of $\overline{\psi} = -0.83$ is considered where Fig. 2 shows ten LS (cf. intersections with $\overline{\psi} = -0.83$). Each of them is taken as a starting solution for a continuation run in υ_0. The criterion (10) is monitored to detect drift bifurcations. After branch switching at these bifurcations also, branches of traveling states are continued. The resulting bifurcation diagram is presented in Fig. 3 with selected solution profiles given in Fig. 4.

We see that the resulting bifurcation curves of steady LS form five separate branches corresponding to different peak numbers between one and five. As before, blue and green branches correspond to odd and even number of peaks, respectively. With increasing activity, the two sub-branches of each branch approach each other till they annihilate at the respective saddle-node bifurcations. This happens first (at the smallest υ_0) for the LS with the largest number of peaks. If time simulations at large values of υ_0 are initialized with such a steady LS, the density peaks decay and the crystallite
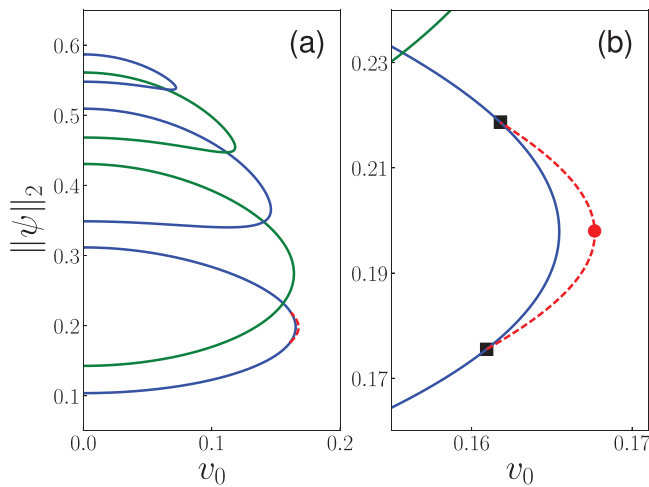
FIG. 3. Panel (a) shows the bifurcation diagram as a function of v_0 at fixed $\overline{\psi} = -0.83$. Line styles of resting states and remaining parameters are as in Fig. 2. Branches of traveling localized states are given as red dashed lines. Panel (b) gives a magnification of the rightmost saddle-node bifurcation of steady LS as there the traveling LS emerge. The filled black square symbols indicate the loci of drift-pitchfork bifurcations, while the red circle marks the example state given in Fig. 4(a). The remaining parameters are $\epsilon = -1.5$, $D_r = 0.5$, $C_1 = 0.1$, $C_2 = 0$, and $L = 100$.

melts into the homogeneous background liquid. The smaller crystallites are slightly more robust, i.e., their annihilating saddle-node bifurcation is at a larger v_0.

Drift-pitchfork bifurcations are only encountered on the branch of one-peak LS. Namely, there is one supercritical drift-pitchfork bifurcation on each sub-branch, both at nearly identical critical values v_c slightly above 0.16 [black squares in Fig. 3(b)].
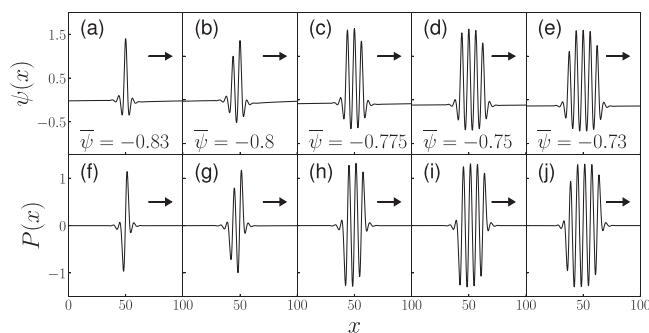

FIG. 4. Density (top) and polarization (bottom) profiles $\psi(x)$ and $P(x)$ of various traveling LS for increasing values of $\overline{\psi}$ at fixed $v_0 = 0.1677$. The peaks travel with a constant velocity. The direction of motion is indicated by the black arrows. Panels (a) and (f) show a profile from the traveling one-peak branch in Fig. 3. Panels (b) and (g) show a traveling two-peak state from Fig. 20, while panels [(c) and (h)], [(d) and (i)], and [(e) and (j)] depict traveling LS with more peaks. The respective values of $\overline{\psi}$ are given in the panels. The remaining parameters as in Fig. 3.

The two drift bifurcations are connected by two branches of traveling one-peak LS that coincide in Fig. 3(b): they consist of κ-asymmetric states that travel in opposite directions and are related to each other by the κ-symmetry that is broken at the drift-pitchfork bifurcation. As expected, close to the bifurcation, the drift velocity $|c|$ shows a square-root behavior. This is the case for all occurring drift-pitchfork bifurcations. The coinciding branches of traveling states are also limited by a saddle-node bifurcation [see magnification in Fig. 3(b)].

All other resting LS melt before motion can set in, i.e., all other saddle-node bifurcations of steady state branches are located at an $v_0 < v_c$. This is confirmed by evaluating the criterion (10): Only the branch of one-peak LS shows zero crossings in the difference of the norms. They occur exactly at the two drift-pitchfork bifurcations.

Inspecting the typical profiles $\psi(x)$ and $P(x)$ of traveling LS in Fig. 4, one clearly notices that the density profile has lost its reflection symmetry and is now slightly asymmetric. In addition, the relative position of $\psi(x)$ and $P(x)$ has changed, i.e., the κ-symmetry is clearly broken. For resting LS, peak maxima in ψ exactly coincide with zeros of P and the resulting inversion symmetry implies that the total polarization (integral of ψ times P over the width of the structure) vanishes, i.e., there is no net polarization. This is not the case for traveling LS where the relative position of $\psi(x)$ and $P(x)$ is shifted and, in consequence, there is a finite net polarization.

Increasing the mean density, more branches of steady LS of successively larger peak number appear and all the limiting saddle-node bifurcations move toward larger v_0. The saddle-node bifurcation where the traveling one-peak LS ends, moves markedly toward larger v_0. Branches of traveling LS of successively larger n appear via drift-pitchfork bifurcations on the corresponding branches of steady LS. The sample profiles of traveling LS are shown in Fig. 4. Further details and bifurcation diagrams at $\overline{\psi} = -0.80$ and $\overline{\psi} = -0.775$ are
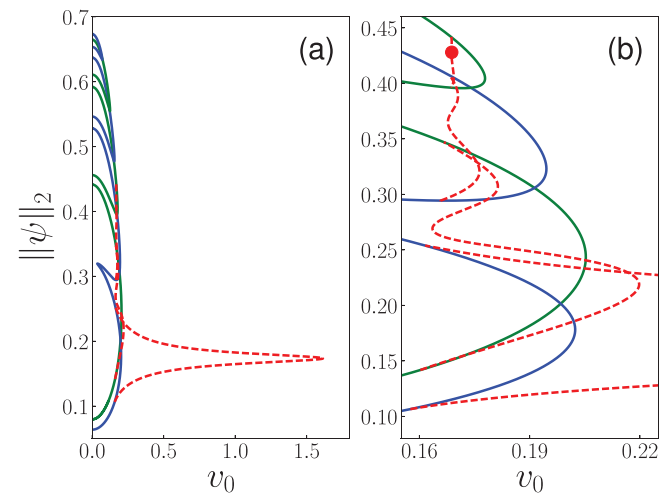
FIG. 5. Panel (a) shows the bifurcation diagram as a function of v_0 at fixed $\overline{\psi} = -0.75$, while (b) magnifies the branches of traveling one- to four-peak LS. Line styles, symbols, and remaining parameters are as in Fig. 3. The corresponding velocities of traveling LS are given in Fig. 6.
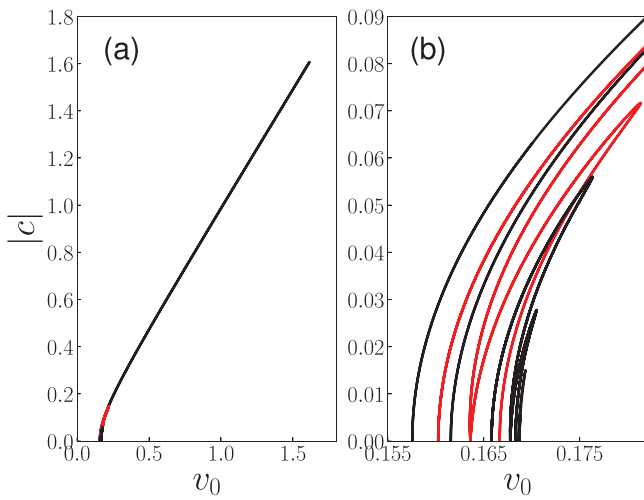
FIG. 6. Panel (a) gives the absolute value of the drift velocity $|c|$ as a function of v_0 for the traveling LS at $\overline{\psi} = -0.75$, i.e., from Fig. 5. Panel (b) magnifies the range where the drift bifurcations occur. Traveling LS with an odd (even) number of peaks are given as black (red)] lines.

given in the Appendix. Figure 5 shows that at $\overline{\psi} = -0.75$, a branch of steady seven-peak LS has emerged as well as a branch of traveling four-peak LS.

Most remarkably, the ranges of existence of the traveling one-peak and two-peak LS have grown to a large extent, while all the other traveling LS are confined to a small v_0-range between $v_0 \approx 0.16$ and $v_0 \approx 0.19$. In particular, the branch of traveling four-peak LS is practically vertical. The saddle-node bifurcation where the traveling one-peak LS terminates has moved out to $v_0 \approx 1.6$. The drift velocities $|c|$ of all traveling LS in Fig. 5 are compared in Fig. 6. We see that for all traveling LS, in the vicinity of the drift-pitchfork bifurcations at respective v_c, as expected, the velocity $|c|$ increases like $|v_0 - v_c|^{1/2}$. At a large $|v_0 - v_c|$, the increase becomes linear. The values v_c increase from about 0.157 to 0.169 as the number of peaks increases from one to four. Note that the velocity of the traveling two- and three-peak LS becomes zero at the end points of the branches (as expected) but also at one respective point in the middle of the branch [at v_0 approximately 0.164 and 0.168, respectively, see Fig. 6(b)]. This indicates that these branches of traveling LS also pass a drift-transcritical bifurcation, where they cross a branch of asymmetric steady LS (not shown here, cf. Ref. 46). In the vicinity of the drift-transcritical bifurcations, c changes linearly.

Further increasing $\overline{\psi}$, more branches of resting and traveling LS appear in the same manner as before. Also, the branches of resting LS of low peak numbers undergo reconnections, e.g., at $\overline{\psi} = -0.73$, the one- and three-peak branches are connected by an additional saddle-node bifurcation. Details of the related pinch-off transition are shown in the Appendix. More importantly, the saddle-node bifurcation where the branch of traveling one-peak LS terminates moves to $v_0 \to \infty$, i.e., drifting LS then exist at arbitrarily high activities. Upon a further increase of $\overline{\psi}$, reconnections

also occur for the branches of traveling states, and isolas of traveling LS appear, shrink, and vanish. Branches of multi-peak traveling LS disappear at saddle-node bifurcation of resting LS. However, the branches of traveling one- and two-peak LS are robust and determine the behavior at large v_0. Further details and bifurcation diagrams are given in Appendix.

The presented study of individual bifurcation diagrams shows how the various branches of resting and traveling localized states emerge, expand, reconnect, shrink, and vanish when increasing the mean density. These glimpses gained at particular values of the mean density are next amplified by considering "existence diagrams" that summarize the behavior in the parameter plane spanned by mean density $\overline{\psi}$ and activity v_0.

C. Existence ranges of resting LS

To obtain an overview where the various resting LS occur in parameter space, we track in Fig. 7 the loci of all saddle-node bifurcations of branches of LS in the plane spanned by activity v_0 and mean density $\overline{\psi}$. At a fixed $\overline{\psi}$, the solid lines give the position of folds of the corresponding branches in bifurcation diagrams with v_0 as the control parameter, e.g., in Figs. 3 and 5. Considering a vertical cut, i.e., fixing a particular constant activity v_0, intersections with the blue and green lines give the loci of folds in bifurcation diagrams with $\overline{\psi}$ as the control parameter, e.g., in Fig. 2. The dotted cyan line tracks the primary bifurcation where the branch of periodic states emerges from the liquid state.

Roughly speaking, each type of resting symmetric LS exists within the region limited by the corresponding solid line. Most of the folds exist only up to $v_0 \approx 0.25$. The final two folds (nearly coinciding blue and green lines in Fig. 7) survive till $v_0 \approx 0.3$. There they
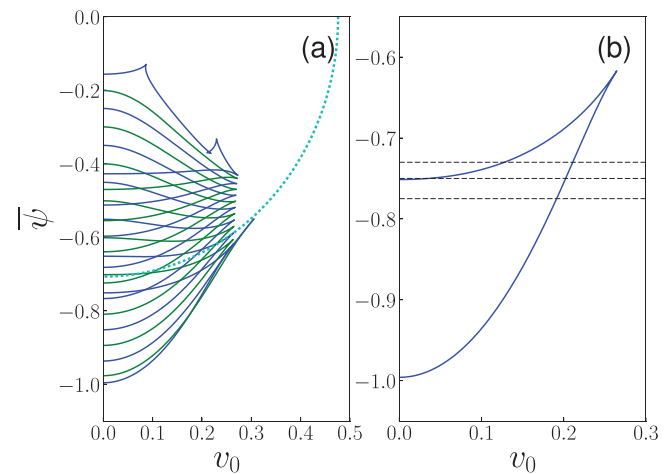
FIG. 7. Panel (a) gives the loci of all saddle-node bifurcations for resting one- to fifteen-peak LS. LS with an odd (even) peak number are given in blue (green), while the primary bifurcation where the resting periodic state emerges is given as the dotted cyan line (corresponding to the red line in Fig. 1). Panel (b) focuses on the loci of the folds of the one-peak LS. Horizontal lines are explained in the main text. The remaining parameters are as in Fig. 3.

vanish at the secondary bifurcation where the two branches of resting symmetric LS emerge from the branch of periodic states. This occurs when this bifurcation changes from subcritical to supercritical. All branches of LS cease to exist at a slightly larger υ_0. The two cusps and the small swallow tail structure of the blue line at the largest $\overline{\psi}$ indicate that reconnections occur in the bifurcation structure. Namely, it depends on the value of υ_0 on which branch of periodic states the branches of LS end: for the passive PFC model ($\upsilon_0 = 0$) at the parameters chosen here, the snaking branches start on the periodic 16-peak state and terminate on the periodic 15-peak state (cf. Fig. 2), whereas for activities larger than $\upsilon_0 \approx 0.12$, they terminate on the periodic 16-peak state. We note in passing that Fig. 7(a) has a very similar appearance as Fig. 6 of Ref. 42 that shows the loci of bifurcations for the passive PFC model in a plane spanned by $\overline{\psi}$ and the effective temperature ϵ. Here, the role of the latter is taken over by the activity υ_0. The implication could be that there exist nonequilibrium analogues of a tricritical point and binodal lines for the present active PFC case. This shall be pursued elsewhere.

Figure 7(b) enlarges a part of Fig. 7(a) focusing only on the one-peak LS. Starting at a low $\overline{\psi}$ and increasing $\overline{\psi}$, the fold moves to the right; hence, the branch of steady one-peak LS exists in a larger range of υ_0. At $\overline{\psi} \approx -0.745$, an additional fold appears at $\upsilon_0 = 0$ and moves toward larger υ_0 with further increasing $\overline{\psi}$. This fold connects the branches of one- and three-peak LS. At $\upsilon_0 = -0.26$, the two-folds annihilate in a hysteresis bifurcation. The dashed horizontal lines indicate values corresponding to the bifurcation diagrams shown in Fig. 22 in the Appendix ($\overline{\psi} = -0.775$), Fig. 5 ($\overline{\psi} = -0.75$), and Fig. 23 in the Appendix ($\overline{\psi} = -0.73$).

D. Existence range of traveling LS

Next, we employ two-parameter continuation to track bifurcations of traveling LS in the ($\upsilon_0, \overline{\psi}$)-plane to obtain an overview of their existence ranges. In this way, we analyze on the one hand the loci of saddle-node bifurcations. On the other hand, we also follow drift-pitchfork bifurcations that mark the onset of motion. Figure 8 gives results for one- and two-peak LS summarizing several properties that we have observed in bifurcation diagrams with either υ_0 or $\overline{\psi}$ as the control parameters. The solid lines give the loci of saddle-node bifurcations. The dashed lines mark the loci of the drift-pitchfork bifurcations, i.e., the onset of motion. Roughly speaking, traveling LS exist in the region between the drift-pitchfork and the saddle-node bifurcations of traveling LS. The information in Fig. 8 is supplemented by Fig. 27 in the Appendix. It additionally presents the corresponding loci of traveling three-peak and four-peak LS. Their region of existence is smaller than the one for one- and two-peak LS.

The tracks of the various bifurcations in the ($\upsilon_0, \overline{\psi}$)-plane can, of course, be related to the previously discussed bifurcation diagrams. Figure 9(a) shows a magnification of Fig. 8 in the region close to the onset of motion. The dashed horizontal and vertical lines highlight the values $\overline{\psi} = -0.75$ and $\upsilon_0 = 0.17$, respectively. The crossings with the horizontal line denote the positions of bifurcations in the bifurcation diagram with the control parameter υ_0 in Fig. 9(b). In an analogous way, the vertical line relates to Fig. 9(c). A close inspection of the three panels indeed shows their full consistency.
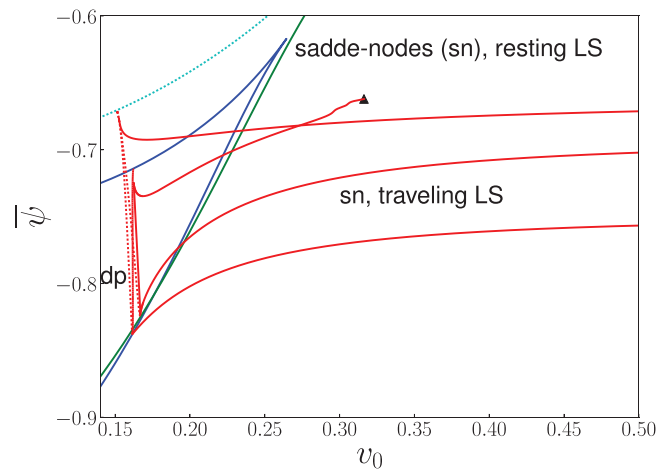

FIG. 8. Shown are the loci of the saddle-node bifurcations ("sn") of resting LS (solid blue and green lines for one-peak and two-peak LS, respectively) and traveling LS (solid red lines) as well as of the drift-pitchfork bifurcations ("dp") where LS start to move (dotted red lines). The loci of the saddle-node bifurcation of the resting periodic state are given as the dotted cyan line. The black triangle marks the point where the investigation of the corresponding branch is terminated as profiles have become seemingly chaotic. A magnification of the region where the drift-pitchfork bifurcations occur is given in Fig. 9. The remaining parameters are as in Fig. 3.

Therefore, we have gained exact knowledge about the parameter region in which a given state exists. As an example, we consider the branch of the one-peak traveling LS: Fig. 9(b) shows that the drift-pitchfork bifurcation named dp_1 marks the onset of motion when increasing υ_0 at a fixed $\overline{\psi}$. Figures 9(b) and 9(c) show that
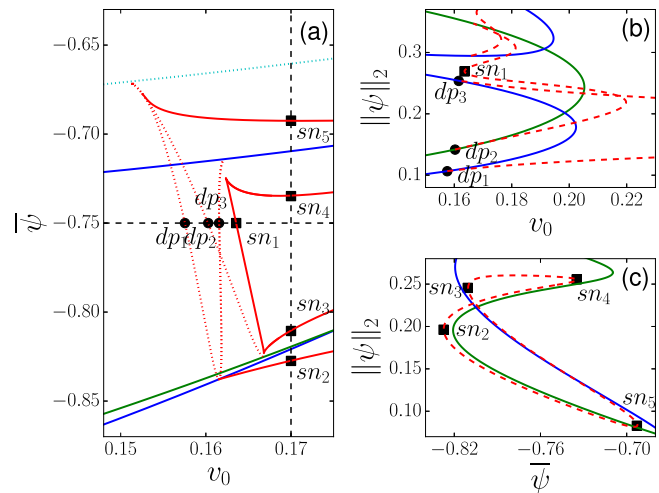

FIG. 9. Panel (a) provides a magnification of the region in Fig. 8 where the drift-pitchfork bifurcations occur. Horizontal and vertical dashed lines highlight the values $\overline{\psi} = -0.75$ and $\upsilon_0 = 0.17$ for which panels (b) and (c) gives the respective one-parameter bifurcation diagrams. Positions of selected drift-pitchfork and saddle-node bifurcations are labeled "dp_i" and "sn_i," respectively.

the saddle-node bifurcations named sn_2 and sn_5 mark the appearance and disappearance of one-peak traveling LS, respectively, when increasing v_0 at a fixed $\overline{\psi}$.

More effects observed in the previous sections can be linked to the results of the bifurcation tracking. For instance, the divergence of the locus of the saddle-node bifurcation limiting the branch of one-peak LS corresponds in Fig. 8 to the fact that the lowest solid red line approaches a horizontal asymptote. The two-parameter continuation also confirms that drift-pitchfork bifurcations are created pairwise together with the connecting branch of traveling LS at the saddle-node bifurcations of resting LS. In Fig. 9(a), this is particularly clearly visible at about $(v_0, \overline{\psi}) \approx (0.1615, -0.8378)$ where red dotted lines (drift-pitchfork bifurcations dp_1 and dp_3) and a red solid line (saddle-node bifurcation of traveling LS sn_2) simultaneously emerge from the blue solid line (saddle-node bifurcation of resting LS)—all for one-peak states.

Note finally that the discontinued branch in Fig. 8 (end marked by a black triangle) corresponds in this region to states that seem chaotic. This is related to the fact that the homogeneous background of the LS is linearly unstable above $\psi \approx -0.6710$. We have not further investigated this region.

E. Morphological phase diagram

In Fig. 10(a), we provide a morphological phase diagram in the plane spanned by activity v_0 and mean density $\overline{\psi}$. It summarizes the ranges of existence of resting and traveling crystalline and LS by combining information gained through linear and nonlinear analyses and direct numerical simulation. The accompanying Fig. 10(b) gives a magnification of the v_0-range close to the onset of motion. The blue and green colored areas indicate where spatially modulated states exist. Thereby the shading encodes the number of density peaks that evolve in the periodic domain of $L = 100 \approx 16 L_c$, where $L_c = 2\pi$. The white regions correspond to the homogeneous liquid state ($\psi = 0$). Spatially extended states that fill the entire domain with 16 peaks are shown in green and occur at a large $\overline{\psi}$.

The initial condition for each time simulation is a single density peak, namely, a Gaussian with oscillatory tails [$\propto \exp(-x^2/5) \cos(x)$]. It is randomly placed on a background of white noise with a small amplitude noise as polarization. After a sufficiently long transient, the number of density peaks is counted for a time interval. Figure 10 shows the median of the peak count (always a natural number). The parameter increments between simulations in Fig. 10(a) are $\Delta v_0 = 0.04$ and $\Delta \overline{\psi} = 0.016$, while for panel (b), $\Delta v_0 = 0.003$ and $\Delta \overline{\psi} = 0.008$ are used.

The solid and dashed white line gives the linear instability threshold with respect to stationary and oscillatory modes, respectively, as determined in Sec. III and shown in Fig. 1. In its vicinity, LS of different sizes exist as indicated by the various shades of blue. Their area of existence is bounded from below by the loci of the folds of the resting and the traveling one-peak LS. They are given as solid and dotted black lines, respectively, cf. Sec. IV D. It is remarkable how well the results from time simulations match the results of parameter continuation. Also note how well the steps in shading in panel (b) indicate the gradual increase in size of the LS with increasing $\overline{\psi}$. Other two-parameter continuations track the onset of motion
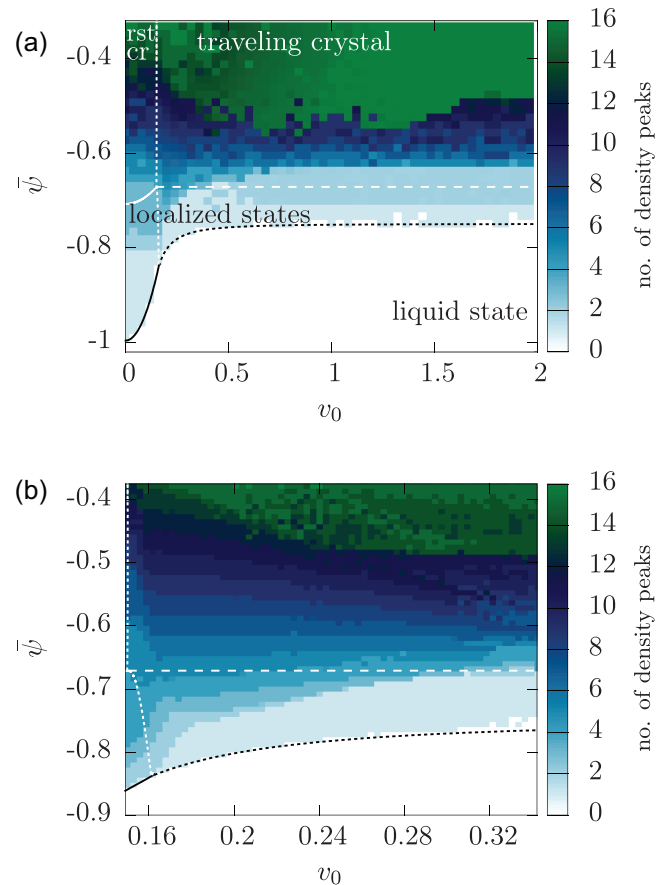

FIG. 10. (a) Morphological phase diagram in the plane spanned by activity v_0 and mean density $\overline{\psi}$. The region of the stable liquid state is white, while crystalline structures of various sizes exist in the colored areas. The color bar indicates the number of density peaks obtained in time simulations. Resting and traveling LS are marked by shades of blue, while domain filling periodic patterns show as green. The various lines in the diagram, the initial conditions of simulations, peak counting and parameter sampling are described in the main text. (b) Magnification of the v_0-range close to the onset of motion. Steps in shading illustrate the gradual growth of LS for increasing $\overline{\psi}$. Remaining parameters are as in Fig. 3.

where resting states undergo a drift-pitchfork bifurcation. The vertical dotted white line marks the onset of motion for crystals. The lower part ($\overline{\psi} < -0.69$) of the nearly vertical line [see magnification in Fig. 10(b)] represents the onset of motion for the one-peak LS.

F. Oscillatory states

The parameter scan performed to obtain Fig. 10 has allowed us to identify additional classes of moving states besides the traveling LS. These are on the one hand oscillating LS that move back and forth without a net drift. They are LS equivalents of the so-called direction reversing traveling waves[80] and have also been observed as, e.g., "wiggling" LS in reaction–diffusion systems[81] or as "creeping"
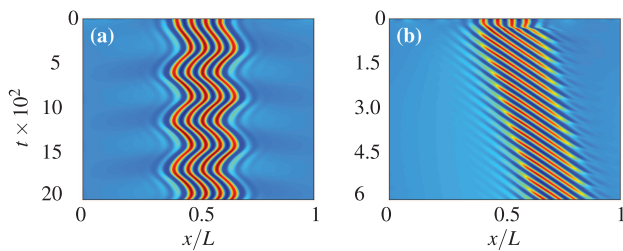
FIG. 11. Panels (a) and (b) show space-time representation of the time evolution of four-peak LS for states II ($v_{Hopf} < v_0 = 0.164 < v_c$) and III ($v_0 = 0.25 > v_c$) in Fig. 12, respectively.

LS in a complex quintic Ginzburg–Landau model.[82] An example with four peaks is given as space–time plot in Fig. 11(a). On the other hand, at a slightly larger v_0, our time simulations result in modulated traveling LS. Similar states are found for binary convection[58,83] where they are called "periodic traveling pulses"[84] or "travelling-wave pulse."[58] Such states exist with different peak numbers close to the linear instability threshold of the uniform phase. An example with four peaks is presented in Fig. 11(b).

Figure 12(a) depicts a corresponding bifurcation diagram in the case of four-peak LS using v_0 as the control parameter, while panel (b) shows selected density and polarization profiles. The diagram is obtained combining the numerical continuation of steady and stationary traveling LS and time simulations of the oscillating direction reversing and modulated traveling LS that could not be obtained by continuation. At low activity, the LS are at rest (blue line, e.g., state I). At about $v_{Hopf} \approx 0.16$ a symmetry-breaking Hopf bifurcation occurs. Time simulations at a slightly larger v_0 with $v_{Hopf} < v_0 < v_c$ exhibit oscillating direction reversing LS [dark red line, e.g., state II, Fig. 11(a)]. At $v_c \approx 0.167$, closely above v_{Hopf}, a drift-pitchfork bifurcation occurs on the branch of resting LS. There, an unstable branch of stationary traveling four-peak LS emerges, as shown as dotted gray line in the inset of Fig. 12(a). It ends at the branch of resting three-peak LS (not shown).

The time simulations indicate that oscillating (direction reversing) states without a net drift exist only in a very narrow range of activity. Beyond this range, time-simulations show modulated traveling states (e.g., state III). The onset of motion occurs close to v_c. In Fig. 12(a), it is indicated by a sudden increase in the time-averaged norm related to the jump onto another branch. The modulated traveling states could be seen as a combination of the destabilized drift and oscillatory modes. However, a simple superposition would lead to a drifting direction-reversing oscillation. Instead, we find a traveling envelope that moves with group velocity c_{group}, while the individual density peaks travel at a larger velocity c_{phase} into the same direction. This implies that peaks are created at the back of the LS and vanish at its tip [Fig. 11(b)]. Similar localized states are described in binary convection where convection cells are generated and destroyed within a traveling pulse envelope.[84]

Increasing v_0 results in a larger difference between c_{group} and c_{phase}. Note that the inset of Fig. 12(a) also indicates a hysteresis between oscillating and modulated traveling LS (light red branch).
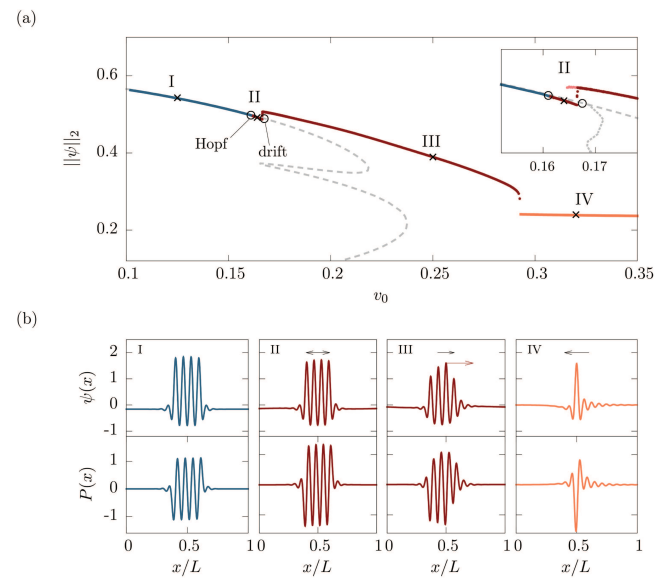

FIG. 12. (a) Bifurcation diagram of four-peak LS obtained by the continuation of steady states (gray dashed line) and time simulations (solid lines): the (time-averaged) norm $||\psi||_2$ is shown as a function of activity v_0. The branch of resting states undergoes a Hopf bifurcation at $v_{Hopf} \approx 0.16$ and a drift instability at $v_c > v_{Hopf}$ (black circles). A region of time-periodic states (red line) starts at v_{Hopf} and ends at a fold bifurcation at $v_0 \approx 0.28$ (for details, see main text). For $v_0 \gtrsim 0.28$, traveling one-peak LS (orange) are found. The inset enlarges the bifurcation structure. Employing time simulations to follow the branch of modulated traveling LS with decreasing v_0 (light red branch in inset) reveals a hysteresis. The branch of traveling four-peak LS (gray dotted, unstable, only shown in inset) emerges at the drift-pitchfork bifurcation at v_c. Panel (b) shows the profiles of selected states at loci marked in panel (a). Directions of motion are indicated by arrows. In particular: (I) resting four-peak LS; (II) oscillating four-peak LS; (III) modulated traveling four-peak LS; (IV) traveling one-peak LS. See Fig. 11 for the space–time plots of (II) and (III). $\overline{\psi} = -0.68$, and the remaining parameters are the same as in Fig. 3.

Due to restrictions of the numerical techniques used, our picture of the details of the transition is incomplete. It is likely that more (unstable) states and possibly global bifurcations are involved.

At another critical activity of $v_0 \approx 0.29$, the branch of modulated traveling four-peak LS seems to fold back as the corresponding curve in Fig. 12(a) seems to approach a vertical. At a larger v_0, time simulations only give traveling one-peak LS (e.g., state IV). To ensure clarity of the diagram, we abstain from including further one-peak branches.

The existence region of modulated traveling LS of different peak numbers is shown in Fig. 13 extracting the pertinent data from the parameter scan performed for Fig. 10. It is constructed by detecting oscillations in the number of density peaks.

Note finally that a bifurcation scenario for various LS involving modulated traveling LS is discussed in Ref. 84 for binary convection. However, it cannot fully clarify where and how the branch of modulated traveling LS emerges. For direction reversing traveling periodic waves, Ref. 80 provides a scenario. It would be particularly interesting to compare the scenarios involving resting, direction reversing
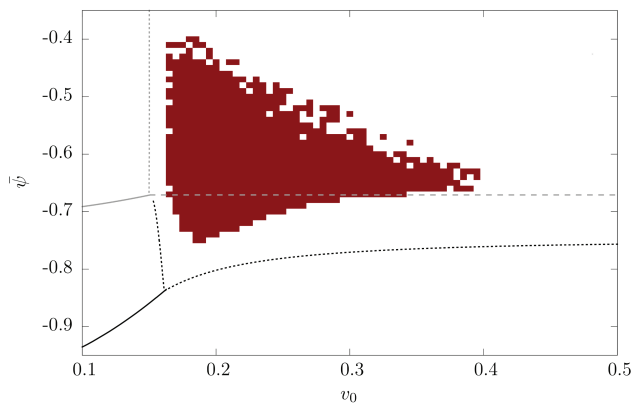
FIG. 13. The shaded region indicates the occurrence of modulated traveling LS of various peak numbers in the plane spanned by activity v_0 and mean density $\overline{\psi}$. Line styles and other details are as in Fig. 10. Oscillating LS (without net drift) appear only in a very narrow v_0-range that is not resolved here.

FIG. 14. Snapshots of the density profile $\psi(x, t)$ of two colliding one-peak LS at $v_0 = 0.5$ and $\overline{\psi} = -0.7$, taken at different times t as indicated in the panels. Arrows in the first and final panel indicate the direction of motion. The LS approach each other with a constant velocity and interact till complete fusion at $t \approx 55$. Then they separate again, i.e., the LS get reflected. Finally, the LS completely recover from the collision and regain their original height and velocity. A space-time plot of this collision is given in Fig. 15(a). The domain size is $L = 100$ and the remaining parameters are as in Fig. 3.

traveling, and modulated traveling LS for systems without conservation law where aligned snaking of steady LS occurs (like Ref. 84) and for systems with conservation law such as the one considered here.

V. INTERACTION OF TRAVELING LS

A. Two colliding LS

Having obtained an extensive description of individual localized states in terms of their bifurcation structure and existence regions in parameter space, we next explore the interaction between LS. A simple way to study such interactions is to look at collision dynamics. First, we examine two colliding one-peak LS. By studying the outcome of collisions, we can distinguish different types of interaction between traveling crystallites. As before, our main control parameters are the activity v_0 (setting the velocity of the colliding crystallites) and the mean density $\overline{\psi}$.

Our typical setup of a numerical collision experiment is as follows. We place two identical traveling one-peak LS with opposite drift velocities at a sufficiently large distance into a domain of length L with periodic boundary conditions and perform a direct time simulation. Due to the periodic boundary conditions, collisions can occur repeatedly allowing us to probe long-time stability. If the colliding LS are initially regularly spaced, the free path λ between two subsequent collisions is $L/2$.

Figure 14 illustrates a typical "elastic" collision of two traveling one-peak LS. Note that "elastic" is used to indicate that the states before and after the collision are identical up to reversed velocities. This is in contrast to an elastic collision in a mechanical system where the kinetic energies before and after the collision are identical. The present nonequilibrium system is overdamped and results from a balance of energy gain (related to a self-propulsion mechanism) and dissipation. No kinetic energy can be assigned to a moving LS.

The snapshots in Fig. 14 show that for $t \lesssim 40$ the LS approach each other at constant velocity, then interact and undergo a deformation that includes a fully fused one-peak intermediate at $t \approx 55$.

Such a state is called "scattor" in Ref. 85. After this momentary fusion, the LS reverse velocity and separate again. Overall, they are eventually reflected and move steadily away from each other from about $t = 60$. Finally, the LS completely recover from the collision and regain their original profile and velocity. This is most clearly seen in the accompanying space-time plot in Fig. 15(a) where the trajectories of the two LS before and after the collision show the same absolute value of the slope. Alternatively, one may describe the interaction as the encounter of two solitary pulses that pass through each other.

Due to the periodic boundary conditions, a sequence of collisions continues *ad infinitum*. For this to occur, the employed domain has to be sufficiently large for the colliding LS to fully recover after a collision before the next one occurs. In consequence, in a system with several LS, each LS needs enough time to recover after each collision to keep a constant number of LS. The recovery time corresponds to a critical free path that needs to be exceeded. This is further discussed below in the context of Fig. 16.

Our main control parameters v_0 and $\overline{\psi}$ strongly influence the outcome of a collision. Figure 15 shows space-time plots of four selected examples that illustrate qualitatively different behavior. Figure 15(a) presents the previously discussed case of two elastically colliding LS. Decreasing $\overline{\psi}$ from -0.7 to -0.75, one finds the interaction shown in Fig. 15(b). The traveling LS interact till they fully merge forming a scattor and then start to move apart again. However, instead of recovering their original properties, they fade away into the linearly stable homogeneous liquid state that forms the background. The overall result of this collision is a complete annihilation of the two LS.

Keeping $\overline{\psi} = -0.75$, a decrease in activity from $v_0 = 0.5$ to $v_0 = 0.2$ (already close to the onset of motion at $v_c \approx 0.16$) gives
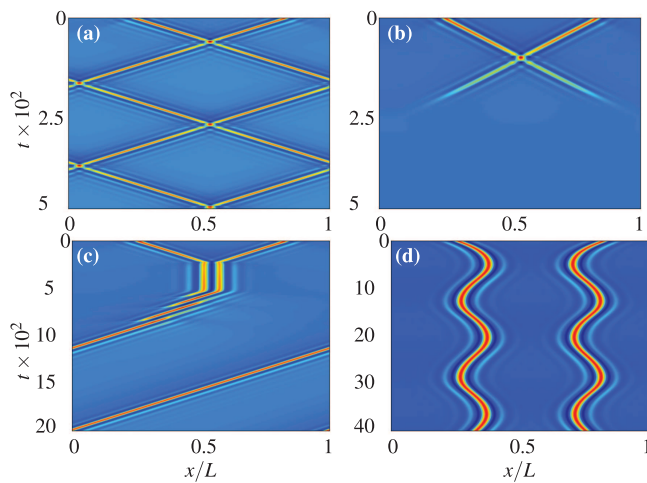
FIG. 15. Shown are space–time plots of the density field $\psi(x)$ for qualitatively different collisions of two one-peak LS. Panel (a) represents the elastic collision at $\upsilon_0 = 0.5$ and $\overline{\psi} = -0.7$ corresponding to Fig. 14; (b) gives an interaction at $\upsilon_0 = 0.5$ and $\overline{\psi} = -0.75$ resulting in a complete annihilation of both LS. Panel (c) shows an inelastic collision at $\upsilon_0 = 0.2$, $\overline{\psi} = -0.75$ resulting in a sequence of unstable resting and modulated traveling two-peak LS and ultimately in a traveling one-peak LS. Finally, panel (d) gives an "avoided collision" at $\upsilon_0 = 0.163$, $\overline{\psi} = -0.71$ where the initial state directly transforms into a state of anti-phase direction-reversing oscillations. In all cases, time increases from top to bottom. The domain size is $L = 100$, and the remaining parameters are the same as in Fig. 14.
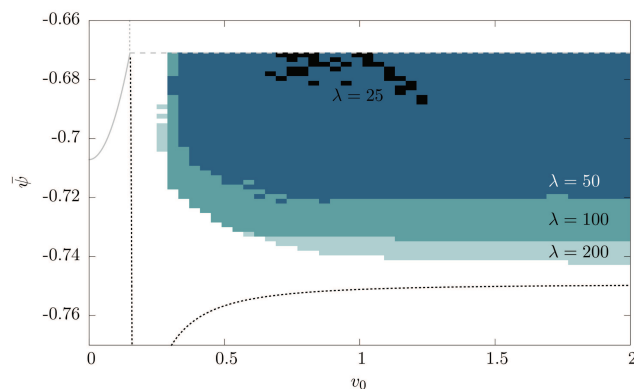
FIG. 16. The occurrence of elastic collisions of one-peak LS in the parameter plane spanned by υ_0 and $\overline{\psi}$ is indicated by the shaded areas for different free path lengths λ. In the white area, collisions are inelastic (or no traveling LS exist), and the number of colliding LS is not conserved. Results for different λ are given as black ($\lambda = 25$), blue ($\lambda = 50$), greenish ($\lambda = 100$), and light gray ($\lambda = 200$) shading. Parameter increments between simulations are $\Delta \upsilon_0 = 0.006$ and $\Delta \overline{\psi} = 0.00125$. The remaining line styles and parameters are as in Fig. 10.

the more intriguing inelastic behavior shown in Fig. 15(c). There, the two traveling LS approach each other, interact but do not merge. Instead, at $t \approx 250$, they come to rest in a bound two-peak state. At first it seems to persist (note the large time scale of the simulation); however, at $t \approx 500$, the state deforms and starts to travel to the left as a modulated traveling two-peak state with $c_{\text{group}} < c_{\text{phase}}$. Again, the state turns out to be an unstable transient, and at $t \approx 800$, a one-peak LS survives that travels with the same speed as the initial LS.

Finally, Fig. 15(d) presents an example at a υ_0 very close to υ_c. The two LS start to approach but then repel each other already long before a proper collision takes place. Subsequently, their motion resembles a periodic anti-phase direction-reversing oscillation. Depending on the type of interacting LS and parameter values, several other cases are possible. However, most occur only in very small parameter ranges and are, therefore, not discussed here.

Similar collision scenarios of LS and transitions between them are discussed for a large number of systems. One example are LS in binary convection,[58,59] that are modeled with coupled Ginzburg–Landau equations[86] and employ the full hydrodynamic model.[87] In Ref. 86, it is demonstrated that there exists an extended parameter range where the interaction is elastic and resembles the collision behavior of conservative integrable systems. However, complete and partial annihilation of LS caused by interaction is also observed. Reference 58 furthermore describes an interaction of LS that results in resting bound states. The interaction of LS is also studied for various reaction–diffusion systems[85,88] and a complex cubic Ginzburg–Landau-like model.[85] Besides elastic collisions, a number of other scattering events are analyzed, including (partial) annihilation, repulsion, fusion, and chaotic dynamics. Similarly, Refs. 89 and 90 discuss the interaction of LS in a three-component reaction–diffusion system. They distinguish generation, annihilation, and scattering of LS as well as the formation of different bound states. The collision of LS with several peaks in a nonvariational cubic-quintic Swift–Hohenberg model is considered in Ref. 91. It seems to always show inelastic behavior. Similar behavior is also found for traveling LS in binary fluid convection.[87] Elastic scattering of LS and the formation of moving LS or resting bound states are also observed in a planar gas-discharge system.[30]

Here, we focus on the prevalent elastic collisions and investigate their occurrence in the parameter plane spanned by υ_0 and $\overline{\psi}$. Again, we initially place two traveling one-peak LS equally spaced on a domain of size L resulting in a free path of $\lambda = L/2$ between collisions. Time simulations are performed for each pair $(\upsilon_0, \overline{\psi})$ at four different values of λ. The resulting parameter map is presented in Fig. 16.

Toward large $\overline{\psi}$, the considered region is limited by the linear instability threshold of the liquid state (horizontal dashed line). Above the line, the uniform state is unstable and spatial modulations grow everywhere. Further details are given below. As before, the nearly vertical dotted line on the left of Fig. 16 marks the onset of motion for one-peak LS and thus represents the lower limit of the investigated υ_0-range. The limit at a low $\overline{\psi}$ is provided by the boundary of the existence region of one-peak LS.

The respective shaded regions indicate where the collision is elastic for the different free path lengths λ. One notices at $\upsilon_0 \approx 0.28$ a rather sharp transition from inelastic to elastic collisions that is

nearly independent of λ. At lower values of v_0, the LS spend too much time in the collision process and lose part of their mass before separating again. If this loss is too large, complete recovery does not occur. At a larger v_0, the LS are faster and spend less time in the actual collision process. This results in a fast complete recovery and long-time conservation of the number of collision partners. One also notices that for elastic collisions to occur, at $\lambda = 50$, the mean density has to exceed a value between $\overline{\psi} \approx -0.71$ and $\overline{\psi} \approx -0.73$, depending on the exact value of $v_0 \gtrsim 0.28$.

Comparing the differently shaded regions in Fig. 16, we note a clear influence of the mean free path λ on the collision behavior. The largest considered free path is $\lambda = 200$ and results in the largest region of elastic collisions. At a large v_0, it nearly coincides with the existence region of traveling one-peak LS. Successively reducing the free path to $\lambda = 100$, $\lambda = 50$, and finally to $\lambda = 25$ results in a decrease in size and finally disappearance of the region of elastic collisions. Interestingly, the above discussed relatively sharp boundary at $v_0 \approx 0.3$ depends only weakly on $\lambda = 50 \ldots 200$. In contrast, the nearly horizontal low-$\overline{\psi}$ limit at a large v_0 with decreasing λ continuously moves toward larger $\overline{\psi}$. For $\lambda < 50$, the change is more dramatic: at $\lambda = 25$, most of the region of elastic collisions

has vanished. This implies that overall, a free path of at least $\lambda \approx 50$ seems necessary for elastic collisions to occur.

Finally, we shed some light on the behavior in the region above the linear stability threshold of the uniform state. Figure 17(a) shows that the area of elastic collisions as determined in Fig. 16 with $\lambda = 50$ reaches well into the linearly unstable region. This is possible because due to mass conservation the presence of the LS lowers the liquid background density, thereby shifting the stability threshold. However, this only holds for a small range of $\overline{\psi}$. The transition from light blue indicating two peaks to darker shading indicates the upper limit of the region of elastic collisions. Increasing $\overline{\psi}$ further leads to the creation of additional spatial modulations in the vicinity of the original LS. Figures 17(b)–17(d) demonstrate selected time evolutions of the colliding density peaks. In panel (b), the initial traveling LS broaden rapidly by developing further peaks. The enlarged structures collide, their envelopes come to rest, while the individual peaks continue to travel with opposing phase velocities. Overall, a localized source-sink structure of peaks is formed. Panel (c) shows a domain-filling traveling crystal with a source of traveling peaks on the boundary and a sink at the center. In panel (d), a state with four density peaks has emerged, all traveling into the
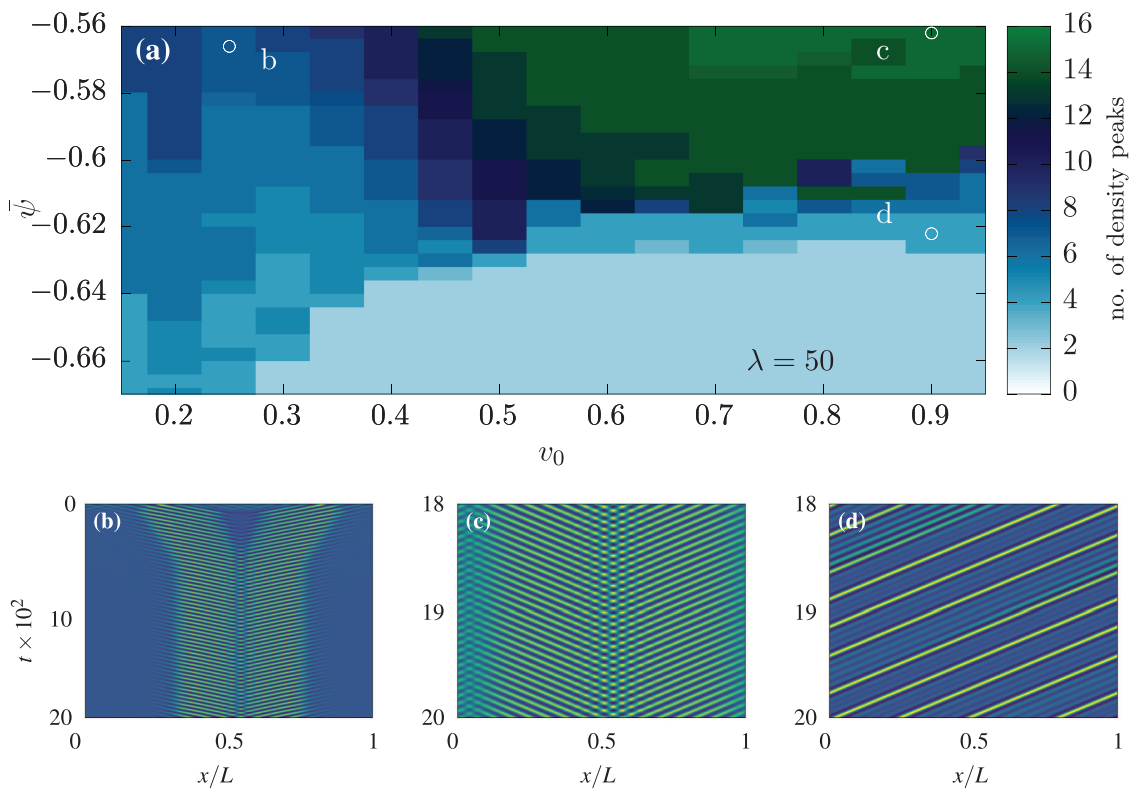

FIG. 17. (a) Morphological phase diagram in the $(v_0, \overline{\psi})$-plane for an initial free path of $\lambda = 50$. Shown is the region above the linear stability threshold of the liquid phase at $\overline{\psi} \approx -0.67$. The initial state corresponds to two traveling one-peak LS on collision course. The long-time outcome is presented in terms of the color-coded number of density peaks. Light blue indicates elastic collisions of two-peak LS. Increasing $\overline{\psi}$, the homogenous background becomes unstable resulting in the formation of an increasing number of peaks. The remaining parameters are as in Fig. 16. Panels (b) to (d) give selected space-time plots of long-time behavior at parameters indicated in panel (a) by letters "b" to "d," respectively.

same direction. The emerging states in panels (b) and (c) show coexistence of traveling waves and standing waves not unlike extended states described for binary fluid convection.[92] Related bursts of traveling waves coexisting with a localized steady pattern are discussed in Ref. 93.

B. Gas of colliding LS in 1D

Based on the obtained results for the elastic collisions of two traveling one-peak LS, we now investigate the behavior of several such LS confined in a large domain. If the number of colliding "particles" is conserved, such a system could be termed a "gas." Figure 18
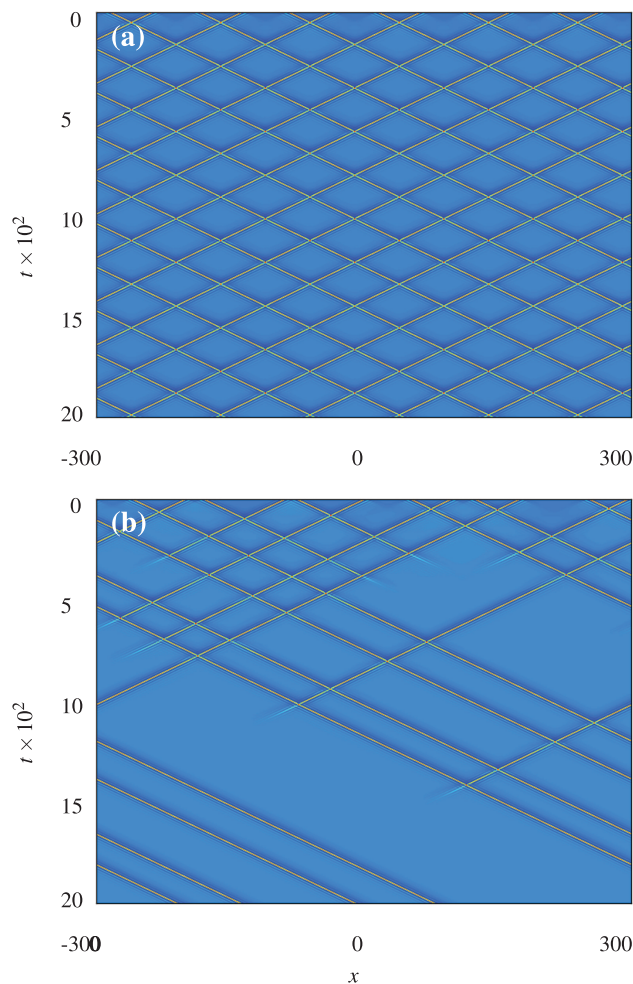
FIG. 18. (a) Space-time plot of a "stable gas" of traveling one-peak LS on a domain with $L = 600$ at $v_0 = 0.5$ and $\bar{\psi} = -0.7$. Twelve one-peak LS are equally spaced on the domain, resulting in a uniform and constant free path of $\lambda = 50$. Panel (b) shows a case where the LS are initially randomly shifted from the regular spacing. As a result, most LS decays after a number of collisions and, eventually, only four LS survive. The remaining parameters are as in Fig. 14.

demonstrates that the minimal free path is crucial for the conservation of the number of LS. Figure 18(a) shows that for initially 12 equally spaced one-peak LS with alternating velocities, a domain of size $L = 600$ provides sufficient space. The corresponding free path of $\lambda = 50$ allows all LS to recover their original properties and to undergo consecutive elastic collisions.

However, this only works if the initial spacing of the LS is regular, as then all trajectories of the ensemble of LS form a regular pattern in the space-time plot, i.e., all collisions are synchronous and all free path lengths are identical and constant across collisions. This is highly unrealistic. In the more realistic situation of LS of varying distances but with the same mean free path one finds the behavior in Fig. 18(b). There, the 12 LS are initially randomly shifted away from the regular spacing. Then, the free path is identical to the previous case and above the critical one; however, not all of the individual free paths are larger than the critical one at all times. This implies that time spans between some of the collisions are too short. The involved LS do not recover their original properties and decay into the homogeneous background. After several collisions the gas is thinned out and consists only of LS traveling with identical speed into the same direction. In the shown example, only four LS survive.

This implies that a stable gas of LS cannot be achieved as in the parameter region where elastic collisions occur, there is no mechanism for the creation of individual peaks out of the uniform background. A possible mechanism could exist beyond the onset of linear instability of the homogeneous background state. However, our investigation in Sec. V A has shown that no individual "free" LS are created in this way but only multi-peak structures showing more complicated collective behavior (see Fig. 17).

VI. CONCLUSION

We have investigated the collision behavior of localized states of the active Phase-Field-Crystal (aPFC) model that combines elements of the Toner–Tu theory for self-propelled particles and the classical Phase-Field-Crystal (PFC) model for the liquid to crystalline phase transition. Based on the results of Ref. 46 on the linear stability of the homogeneous liquid state, and the existence and onset of motion of space-filling crystals and selected crystallites, i.e., localized states, we have first studied the bifurcation structure and existence regions of various traveling localized states in detail. This has allowed us to identify oscillating and modulated traveling localized states. Like the traveling localized states, they have no counterpart in the classical PFC model that only allows for resting states.

The results of linear stability analyses, two-parameter continuation, and direct time simulations have been combined to obtain morphological phase diagrams in the parameter plane spanned by activity and mean density. They indicate where the various resting and traveling localized states exist. This has allowed us to identify the parameter region where the collision behavior of traveling one-peak localized states can be analyzed. As a result, we have distinguished elastic and inelastic collisions. In the elastic case, the localized states eventually recover their properties after a collision. In contrast, in the inelastic case, the localized states may completely or partially annihilate, forming resting bound states or various traveling states. This occurs at all studied parameter values if a certain minimal free

path is no longer guaranteed. We have shown that this rules out the possibility of a stable "gas" of localized states, as in such a gas, there is always a spectrum of different free paths. This results in the annihilation of localized states if one does not use highly artificial regular initial conditions.

There remains a number of questions that merit further investigation. First, the bifurcation behavior related to the emergence of the newly identified direction reversing oscillating and modulated traveling localized aPFC states should be clarified. This has remained beyond the scope of the present work, but this is done for several time-periodic spatial structures in reaction–diffusion systems.[81] Continuation techniques are employed for (simpler) systems of driven[94,95] or active matter.[78] Ultimately, this should contribute to a more systematic understanding of mechanisms that result in the onset of motion in various systems of active matter described by nonvariational models.[96–98]

Second, it will be very instructive to expand the present study toward two- and three-dimensional systems as done for the classical passive PFC model in Refs. 42, 62, and 77 or for reaction–diffusion systems in Refs. 31, 90, and 99. However, an increase in dimensionality will result in a much richer bifurcation behavior as there are more symmetries that can be broken. This may, for instance, result in the occurrence of drift bifurcations for the onset of translation (as in the present one-dimensional case) and also for rotation similar to transitions observed for LS in reaction–diffusion systems.[100]

As an outlook, we consider an example for the collision behavior in two spatial dimensions that allows us to point out certain features and may serve as a starting point for future studies. Figure 19 shows snapshots of a simulation initialized with six randomly placed one-peak LS that travel with a constant speed of $c \approx 0.15$ in various directions (according to an activity of $v_0 = 0.2$). Interestingly, the collision behavior is much more robust than in the 1D case.
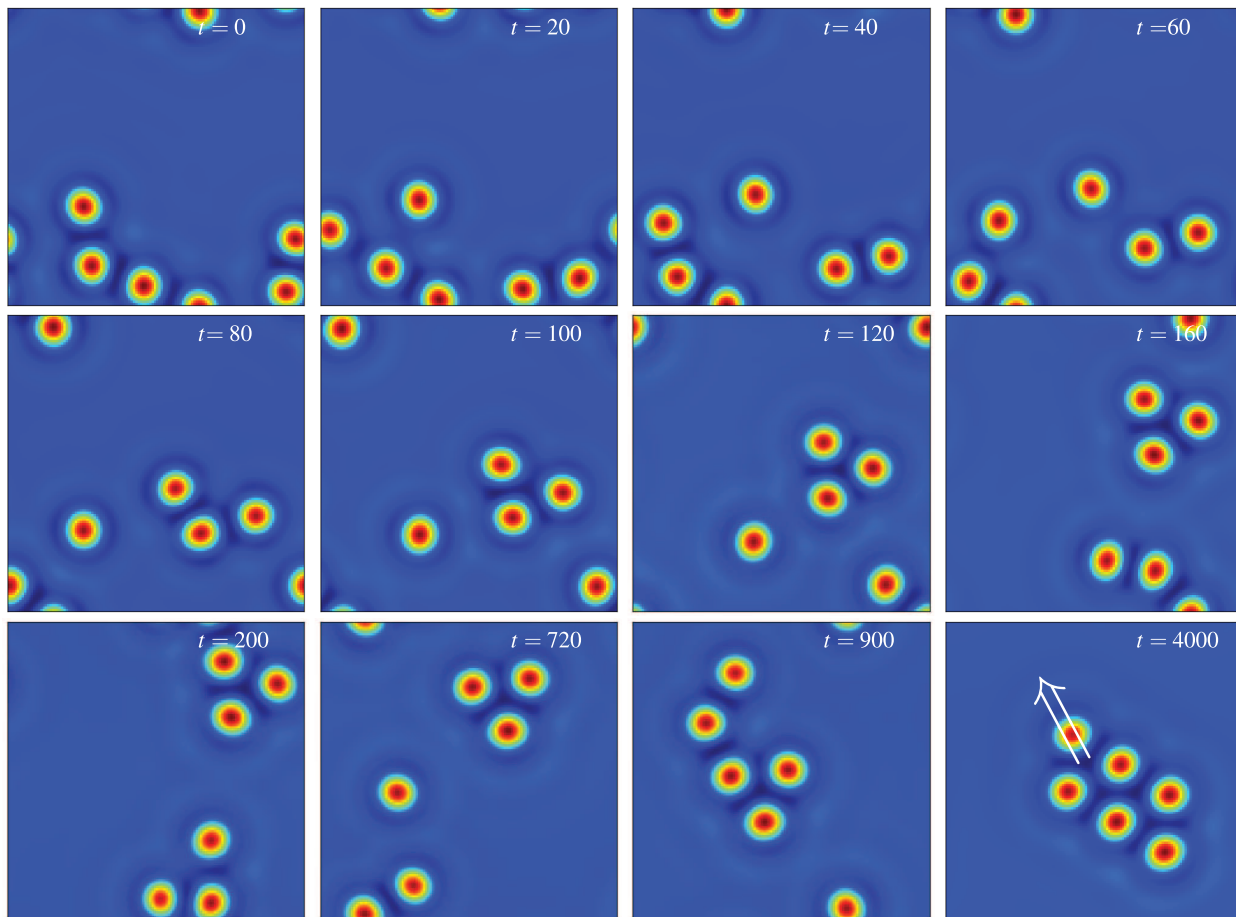
FIG. 19. Time series of snapshots showing the collision and condensation dynamics of six traveling LS at $v_0 = 0.2$ and $\overline{\psi} = -0.8$. Shown is the density profile $\psi(\mathbf{x}, t)$ at times t as given in the panels. The domain size is $L_x \times L_y = 32\pi/\sqrt{3} \times 14\pi$ and has periodic boundaries. Note that all LS are in motion at all times. Remaining parameters are as in Fig. 14.

We find that the number of peaks remains constant through the various collisions. In contrast to the 1D case, after the first collisions (from $t \approx 50$), the one-peak LS "condense" into larger clusters, first into two- and three-peak LS (the latter emerges at $t \approx 100$) and finally into a six-peak LS ($t = 4000$). Within the cluster, the density peaks form a hexagonal pattern. The white arrow indicates the direction of motion and is oriented perpendicularly to one side of the equilateral triangle at the tip of the cluster. Before this direction of translation emerges, rotational modes are visible and the direction of the collective drift keeps changing.

Such a dynamical coalescence of active particles into extended clusters that move as one entity is also observed in experiments. For instance, in Ref. 101, carbon-coated colloidal Janus particles are dispersed in a mixture of water and lutidine and move with a speed depending on the intensity of illumination. There, the formation of larger clusters is a dynamical process and is counteracted by the break up of clusters. It will be interesting to investigate whether such breakup processes can also occur in the dynamics of ensembles of LS in the active PFC model.

AUTHORS' CONTRIBUTIONS

L.O. and J.K. contributed equally to this work.

APPENDIX: ADDITIONAL BIFURCATION DIAGRAMS FOR RESTING AND TRAVELING LS

In this Appendix, we supplement the information given in Sec. IV B regarding the bifurcation structure of resting and traveling localized states (LS). In particular, we present additional bifurcation diagrams to allow the interested reader to better follow the various changes in their structure that occur with increasing mean density $\overline{\psi}$.

First, we increase the mean density from $\overline{\psi} = -0.83$ of Fig. 3 to $\overline{\psi} = -0.80$. Then, there are 12 steady LS at $\upsilon_0 = 0$ (cf. Fig. 2) as an additional branch of resting six-peak LS has appeared above the other branches. The resulting bifurcation diagram over υ_0 is given in Fig. 20. The branches of steady n-peak LS are qualitatively similar to the previous case of $\overline{\psi} = -0.83$ (Fig. 3); only the annihilating saddle-node bifurcations have moved to a slightly larger υ_0, and the range of represented norms is larger. More importantly, the saddle-node bifurcation where the traveling one-peak LS ends has moved markedly to the right, i.e., the υ_0-range of their existence is much larger than before. Most remarkably, a second branch of traveling LS has come into existence that consists of two-peak states. Its structure is more involved than the one of the one-peak states, as it undergoes three saddle-node bifurcations. However, these states only exist in
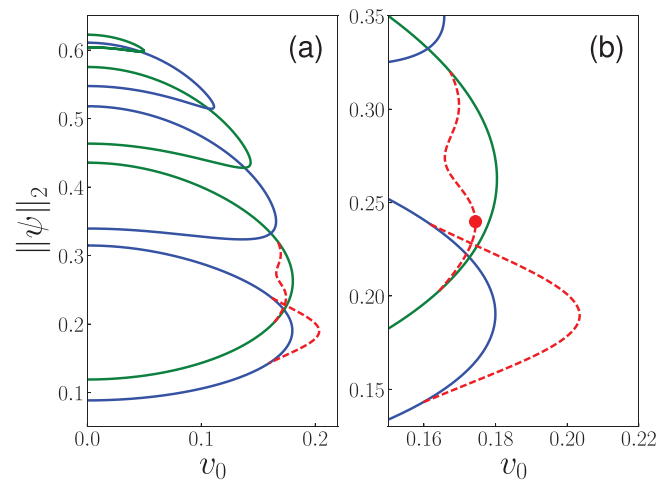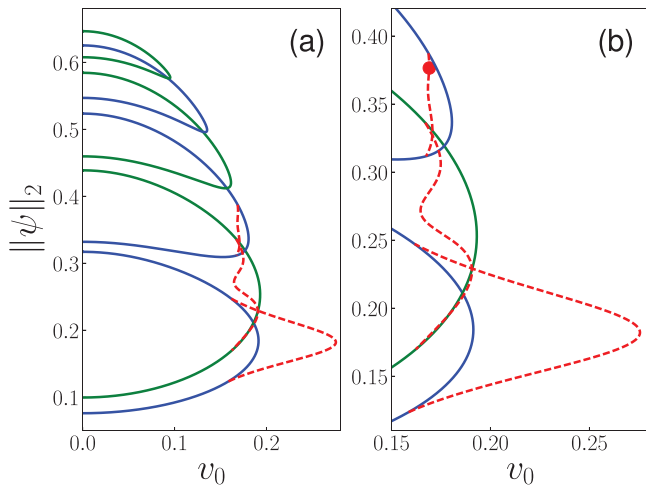

FIG. 20. Panel (a) shows the bifurcation diagram as a function of υ_0 at a fixed $\overline{\psi} = -0.80$, while (b) magnifies the branches of traveling LS. Line styles, symbols, and remaining parameters are as in Fig. 3.

a small υ_0-range, and the whole branch lies within the region limited by the branch of steady two-peak LS. The profiles of a sample traveling two-peak LS are shown in Figs. 4(b) and 4(g).

As the branch of traveling two-peak LS in Fig. 20 has a nontrivial form, we further investigate its metamorphosis with increasing $\overline{\psi}$. Figure 21 shows four intermediate stages between Figs. 3 and 20. From this, it is clear that the traveling two-peak branch emerges (as does the branch of traveling one-peak states) via the simultaneous creation of two drift-pitchfork bifurcations at the saddle-node bifurcation of the resting LS (cf. top left panel of Fig. 21 at $\overline{\psi} = -0.824$.
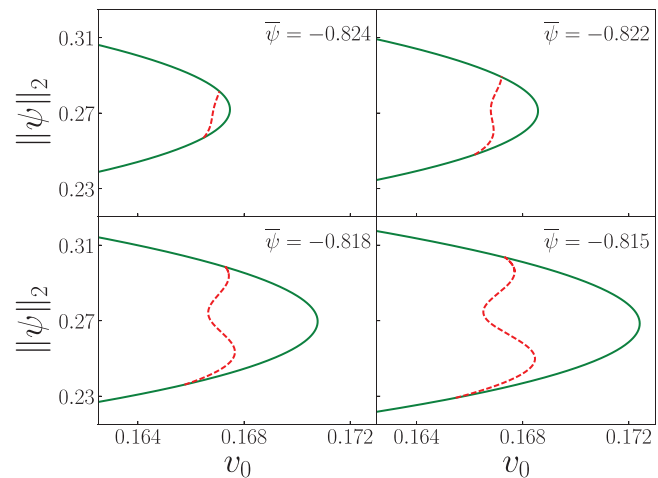
FIG. 21. To demonstrate how traveling two-peak LS emerge, a sequence of bifurcation diagrams of two-peak LS is given for mean densities between the ones of Figs. 3 and 20, namely, for $\overline{\psi} = -0.824, -0.822, -0.818,$ and -0.815 (from top left to bottom right). Line styles and remaining parameters are as in Fig. 3.

FIG. 22. Panel (a) shows the bifurcation diagram as a function of v_0 at fixed $\overline{\psi} = -0.775$, while (b) magnifies the branches of traveling one-peak, two-peak and three-peak LS. Line styles, symbols, and remaining parameters are as in Fig. 3.
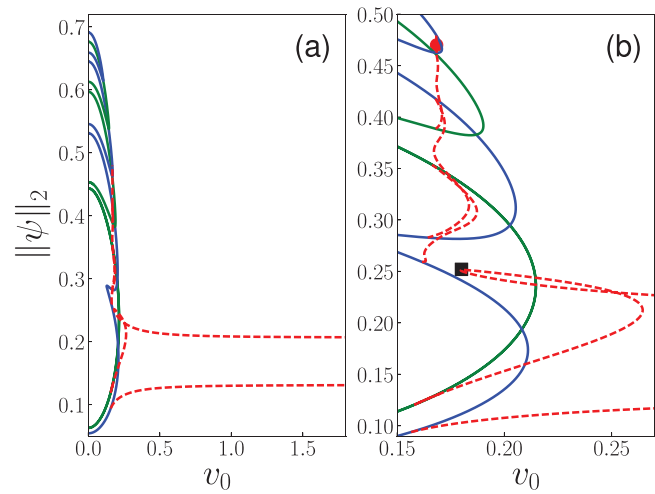
FIG. 23. Panel (a) shows the bifurcation diagram as a function of v_0 at fixed $\overline{\psi} = -0.73$, while (b) magnifies the branches of traveling one- to five-peak LS. Traveling one-peak LS exist now for arbitrarily large activity. Here, the black square indicates the newly formed saddle-node bifurcation resulting from the pinch-off bifurcation. Remaining line styles, symbols, and parameters are as in Fig. 3.

As $\overline{\psi}$ increases, saddle-node bifurcations appear on the branch through a hysteresis bifurcation and a transition from a supercritical to a subcritical drift-pitchfork bifurcation.

Increasing the mean density to $\overline{\psi} = -0.775$, we find the bifurcation diagram in Fig. 22. In contrast to the previous case, the branch of resting three-peak LS now reaches activities high enough to result in the emergence of a branch of traveling three-peak LS. Its creation is identical to that of the branch of traveling two-peak LS, cf. Fig. 21. However, the traveling three-peak LS exist only in a very narrow range of v_0. A sample solution profile of a traveling three-peak LS is given in Fig. 4.

A further increase to $\overline{\psi} = -0.75$ results in the bifurcation diagram presented in Fig. 5 in Sec. IV B. Changes include the appearance of a branch of steady seven-peak LS and a branch of traveling four-peak LS and are discussed in the main text.

At $\overline{\psi} = -0.73$, see Fig. 23, the branches of resting one- to five-peak LS exist and each of them is the source of a branch of traveling LS, i.e., they also exist with one to five peaks. Two further remarkable changes have occurred. First, the bifurcation structure of the branches of traveling one-peak and three-peak states has changed. They are now connected by an additional saddle-node bifurcation at $v_0 \approx 0.18$ [Fig. 23(b)]. Details of the pinch-off transition occurring between $\overline{\psi} = -0.736$ and $\overline{\psi} = 0.734$ at $v_0 \approx 0.17$ can be discerned in Fig. 24, where a series of bifurcation diagrams focuses on the relevant changes occurring between Figs. 5 and 23. We see that for increasing $\overline{\psi}$ the two nearly aligned parts of the two branches approach each other until they touch and reconnect. There is now an "open loop" that is disconnected from the branches of resting LS. At pinch-off, two saddle-node bifurcations are created. Their separation increases with increasing $\overline{\psi}$ and the one on the left hand side soon merges into the remaining drift-pitchfork bifurcation.

Second and most importantly, the position of the saddle-node bifurcation where the branch of traveling one-peak LS terminates at a high v_0 has diverged to $v_0 \to \infty$, i.e., these traveling states now exist at arbitrarily high activities (and can reach corresponding velocities).

The final increase in mean density that we consider here, brings us to $\overline{\psi} = -0.71$, see Fig. 25. Compared with $\overline{\psi} = -0.73$ (Fig. 23),
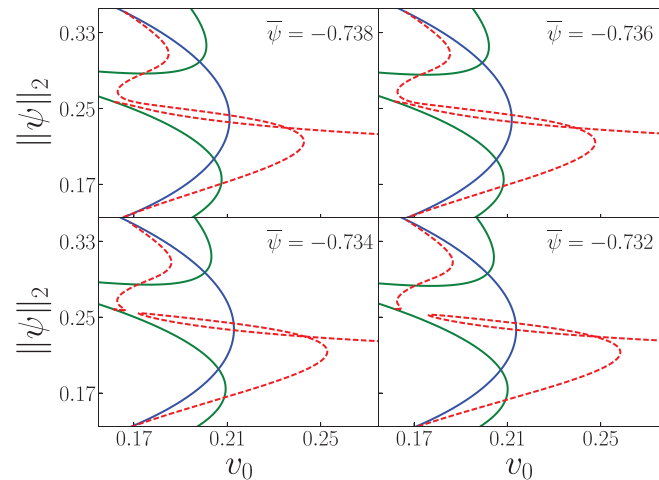

FIG. 24. A series of bifurcation diagrams focusing on the pinch-off bifurcation involving the branches of traveling one- and two-peak LS. Diagrams for $\overline{\psi} = -0.738, -0.736, -0.734,$ and -0.732 (from top left to bottom right) are shown. Line styles and remaining parameters are as in Fig. 3.
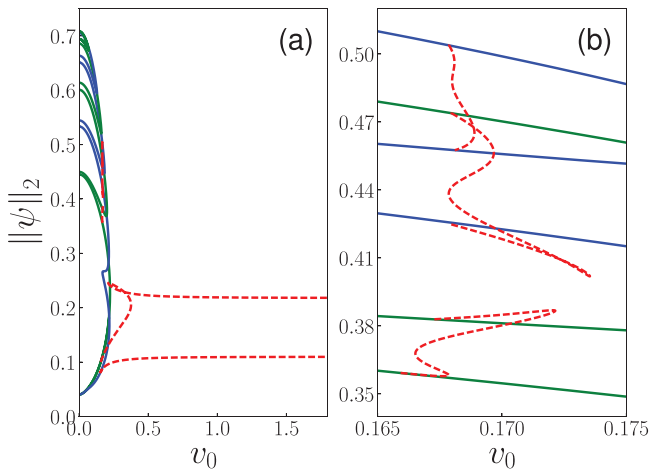
FIG. 25. Panel (a) shows the bifurcation diagram as a function of v_0 at fixed $\overline{\psi} = -0.71$, while (b) magnifies the branches of traveling three- to five-peak LS. Traveling one-peak LS still exist for an arbitrarily high activity. Remaining line styles, symbols, and parameters are as in Fig. 3.

an additional branch of resting eight-peak LS has appeared. Also, the bifurcation structure of the branches of traveling LS is now partly dissolving due to further pinch-off bifurcations. To obtain an impression, see the sequence of magnifications at different $\overline{\psi}$
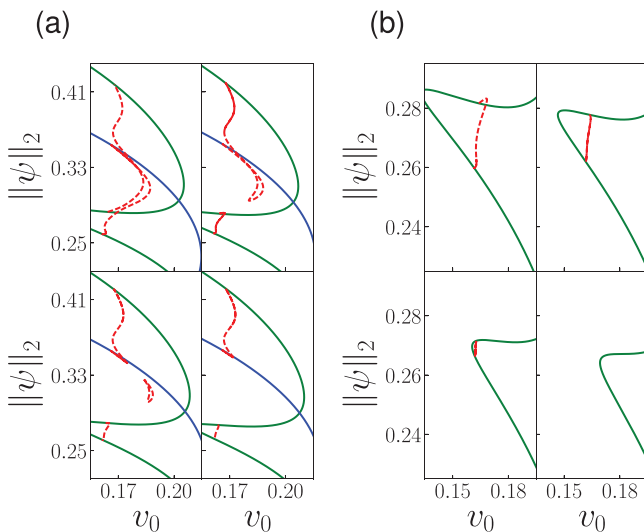
FIG. 26. Details are given for the intricate bifurcation processes occurring between $\overline{\psi} = -0.73$ (Fig. 23) and $\overline{\psi} = -0.71$ (Fig. 25). Panel (a) focuses on the pinch-off bifurcation of traveling two- and three-peak LS and shows magnifications for $\overline{\psi} = -0.730, -0.727, -0.724,$ and -0.721 (from top left to bottom right) where even isolas of traveling LS are created. Panel (b) shows how the traveling two-peak LS disappears with increasing $\overline{\psi} = -0.728, -0.722, -0.715,$ and -0.710 (from top left to bottom right). Line styles and remaining parameters are as in Fig. 3.
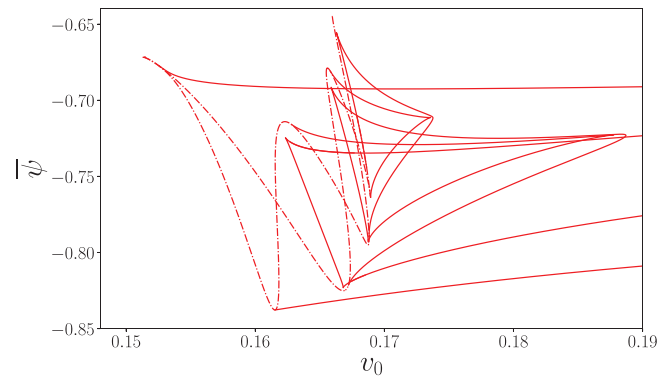
FIG. 27. Loci of the saddle-node and drift-pitchfork bifurcations of traveling localized one-, two-, three-, and four-peak states (not distinguished) from two-parameter continuation. Saddle-node bifurcations are given by solid lines and drift-pitchfork bifurcations by dotted-dashed lines. Remaining parameters are as in Fig. 3.

given in Fig. 26(a). Note that an isola of traveling LS is created by two pinch-off bifurcations. Upon a further increase of $\overline{\psi}$, this isola shrinks and disappears in another codimension-2 bifurcation. Figure 26(b) illustrates with a sequence of magnifications at different $\overline{\psi}$ how another branch of traveling LS first straightens, then shrinks in length by moving toward a saddle-node bifurcation of resting LS that finally entirely absorbs it. In this way, many of the multi-peak traveling LS disappear. However, the branches of traveling one- and two-peak LS are robust and determine the behavior at a large v_0 (cf. Fig. 25).

The presented study of individual bifurcation diagrams has shown how the various branches of resting and traveling localized states emerge, expand, reconnect, shrink, and vanish upon changing the mean density.

These glimpses gained in the Appendix and in Sec. IV B at particular values of the mean density are amplified in Secs. IV C and IV D by considering the behavior in the parameter plane spanned by mean density $\overline{\psi}$ and activity v_0.

Finally, Fig. 27 supplements the existence diagrams given in Figs. 8 and 9 of the main text. Figure 27 not only includes the saddle-node bifurcations and drift-pitchfork bifurcations of one- and two-peak LS but also adds the corresponding loci of traveling three-peak and four-peak LS. Their region of existence is smaller than the one for the one- and two-peak states. This completes the overview of steady and traveling LS.

DATA AVAILABILITY

The data that support the findings of this study are openly available in Zenodo at https://doi.org/10.5281/zenodo.4322992.[102]

REFERENCES

[1] P. Ball, *The Self-Made Tapestry: Pattern Formation in Nature* (Oxford University Press, 1999).
[2] L. Lam, *Nonlinear Physics for Beginners: Fractals, Chaos, Solitons, Pattern Formation, Cellular Automata, Complex Systems* (World Scientific, 1998).

[3]L. M. Pismen, *Patterns and Interfaces in Dissipative Dynamics*, Springer Series in Synergetics (Springer, 2006).

[4]C. Misbah, *Complex Dynamics and Morphogenesis: An Introduction to Nonlinear Science* (Springer, Netherlands, 2017).

[5]M. C. Cross and P. C. Hohenberg, Rev. Mod. Phys. **65**, 851 (1993).

[6]H. Wada and R. R. Netz, Phys. Rev. Lett. **99**, 108102 (2007).

[7]W.-J. Rappel, A. Nicol, A. Sarkissian, H. Levine, and W. F. Loomis, Phys. Rev. Lett. **83**, 1247 (1999).

[8]B. Szabó, G. J. Szöllösi, B. Gönci, Z. Jurányi, D. Selmeczi, and T. Vicsek, Phys. Rev. E **74**, 061908 (2006).

[9]D. J. Sumpter, *Collective Animal Behavior* (Princeton University Press, Princeton, 2010).

[10]M. C. Marchetti, J. F. Joanny, S. Ramaswamy, T. B. Liverpool, J. Prost, M. Rao, and R. A. Simha, Rev. Mod. Phys. **85**, 1143 (2013).

[11]C. Bechinger, R. Di Leonardo, H. Löwen, C. Reichhardt, G. Volpe, and G. Volpe, Rev. Mod. Phys. **88**, 045006 (2016).

[12]N. Uchida and R. Golestanian, Phys. Rev. Lett. **106**, 058104 (2011).

[13]R. Golestanian, J. M. Yeomans, and N. Uchida, Soft Matter **7**, 3074 (2011).

[14]J. Palacci, S. Sacanna, A. P. Steinberg, D. J. Pine, and P. M. Chaikin, Science **339**, 936 (2013).

[15]H.-R. Jiang, N. Yoshinaga, and M. Sano, Phys. Rev. Lett. **105**, 268302 (2010).

[16]W. Wang, L. A. Castro, M. Hoyos, and T. E. Mallouk, ACS Nano **6**, 6122 (2012).

[17]J. Voß and R. Wittkowski, Nanoscale Adv. **2**, 3890 (2020).

[18]J. R. Howse, R. A. L. Jones, A. J. Ryan, T. Gough, R. Vafabakhsh, and R. Golestanian, Phys. Rev. Lett. **99**, 048102 (2007).

[19]S. A. Mallory, C. Valeriani, and A. Cacciuto, Ann. Phys. Chem. **69**, 59 (2018).

[20]F. Ginot, I. Theurkauff, D. Levis, C. Ybert, L. Bocquet, L. Berthier, and C. Cottin-Bizonne, Phys. Rev. X **5**, 011004 (2015).

[21]A. P. Solon, J. Stenhammar, R. Wittkowski, M. Kardar, Y. Kafri, M. E. Cates, and J. Tailleur, Phys. Rev. Lett. **114**, 198301 (2015).

[22]M. E. Cates and J. Tailleur, Annu. Rev. Condens. Matter Phys. **6**, 219 (2015).

[23]R. Thar and M. Kühl, Appl. Environ. Microbiol. **68**, 6310 (2002).

[24]R. Thar and M. Kühl, FEMS Microbiol. Lett. **246**, 75 (2005).

[25]I. Theurkauff, C. Cottin-Bizonne, J. Palacci, C. Ybert, and L. Bocquet, Phys. Rev. Lett. **108**, 268303 (2012).

[26]A. P. Petroff, X.-L. Wu, and A. Libchaber, Phys. Rev. Lett. **114**, 158102 (2015).

[27]F. Ginot, I. Theurkauff, F. Detcheverry, C. Ybert, and C. Cottin-Bizonne, Nat. Commun. **9**, 696 (2018).

[28]J. Toner, Y. Tu, and S. Ramaswamy, Ann. Phys. **318**, 170 (2005).

[29]B. M. Mognetti, A. Saric, S. Angioletti-Uberti, A. Cacciuto, C. Valeriani, and D. Frenkel, Phys. Rev. Lett. **111**, 245702 (2013).

[30]Y. A. Astrov and H.-G. Purwins, Phys. Lett. **283**, 349 (2001).

[31]H. G. Purwins, H. U. Bödeker, and S. Amiranashvili, Adv. Phys. **59**, 485 (2010).

[32]U. Bortolozzo, M. G. Clerc, and S. Residori, New J. Phys. **11**, 093037 (2009).

[33]A. M. Menzel, Phys. Rep. **554**, 1 (2015).

[34]H. Reinken, S. H. L. Klapp, M. Bär, and S. Heidenreich, Phys. Rev. E **97**, 022613 (2018).

[35]J. Toner and Y. Tu, Phys. Rev. Lett. **75**, 4326 (1995).

[36]J. Toner and Y. Tu, Phys. Rev. E **58**, 4828 (1998).

[37]A. M. Menzel and H. Löwen, Phys. Rev. Lett. **110**, 055702 (2013).

[38]K. R. Elder, M. Katakowski, M. Haataja, and M. Grant, Phys. Rev. Lett. **88**, 245701 (2002).

[39]H. Emmerich, H. Löwen, R. Wittkowski, T. Gruhn, G. I. Tóth, G. Tegze, and L. Gránásy, Adv. Phys. **61**, 665 (2012).

[40]G. Tegze, L. Gránásy, G. I. Tóth, F. Podmaniczky, A. Jaatinen, T. Ala-Nissila, and T. Pusztai, Phys. Rev. Lett. **103**, 035702 (2009).

[41]K. R. Elder, G. Rossi, P. Kanerva, F. Sanches, S. C. Ying, E. Granato, C. V. Achim, and T. Ala-Nissila, Phys. Rev. Lett. **108**, 226102 (2012).

[42]U. Thiele, A. J. Archer, M. J. Robbins, H. Gomez, and E. Knobloch, Phys. Rev. E **87**, 042915 (2013).

[43]E. Knobloch, IMA J. Appl. Math. **81**, 457 (2016).

[44]A. M. Menzel, T. Ohta, and H. Löwen, Phys. Rev. E **89**, 022301 (2014).

[45]A. I. Chervanyov, H. Gomez, and U. Thiele, Europhys. Lett. **115**, 68001 (2016).

[46]L. Ophaus, S. V. Gurevich, and U. Thiele, Phys. Rev. E **98**, 022608 (2018).

[47]J. D. Murray, *Mathematical Biology* (Springer, Berlin, 1993).

[48]H. Meinhardt, *Models of Biological Pattern Formation* (Academic Press, London, 1982).

[49]P. Coullet, C. Riera, and C. Tresser, Phys. Rev. Lett. **84**, 3069 (2000).

[50]*Chemical Waves and Patterns*, Understanding Chemical Reactivity Vol. 10, edited by R. Kapral and K. Showalter (Kluwer Academic Publishers, Dordrecht, 1995).

[51]V. K. Vanag and I. R. Epstein, Chaos **17**, 037110 (2007).

[52]J. Burke and E. Knobloch, Phys. Rev. E **73**, 056211 (2006).

[53]N. Akhmediev and A. Ankiewicz, *Dissipative Solitons: From Optics to Biology and Medicine Series*, Lecture Notes in Physics Vol. 751 (Springer, Berlin, Heidelberg, 2008).

[54]M. Tlidi and P. Mandel, Phys. Rev. Lett. **83**, 4995 (1999).

[55]E. Meron, H. Yizhaq, and E. Gilad, Chaos **17**, 037109 (2007).

[56]R. Richter and I. V. Barashenkov, Phys. Rev. Lett. **94**, 184503 (2005).

[57]B. Schäpers, M. Feldmann, T. Ackemann, and W. Lange, Phys. Rev. Lett. **85**, 748 (2000).

[58]P. Kolodner, Phys. Rev. A **44**, 6466 (1991).

[59]J. A. Glazier and P. Kolodner, Phys. Rev. A **43**, 4269 (1991).

[60]O. Lioubashevski, Y. Hamiel, A. Agnon, Z. Reches, and J. Fineberg, Phys. Rev. Lett. **83**, 3190 (1999).

[61]M. J. Robbins, A. J. Archer, U. Thiele, and E. Knobloch, Phys. Rev. E **85**, 061408 (2012).

[62]S. Engelnkemper, S. V. Gurevich, H. Uecker, D. Wetzel, and U. Thiele, in *Computational Modeling of Bifurcations and Instabilities in Fluid Mechanics*, Computational Methods in Applied Sciences Vol 50, edited by A. Gelfgat (Springer, 2019), pp. 459–501.

[63]J. Burke and E. Knobloch, Chaos **17**, 037102 (2007).

[64]M. Beck, J. Knobloch, D. J. B. Lloyd, B. Sandstede, and T. Wagenknecht, SIAM J. Math. Anal. **41**, 936 (2009).

[65]U. Bortolozzo, M. G. Clerc, and S. Residori, Phys. Rev. E **78**, 036214 (2008).

[66]J. H. P. Dawes, SIAM J. Appl. Dyn. Syst. **7**, 186 (2008).

[67]D. Lo Jacono, A. Bergeon, and E. Knobloch, J. Fluid Mech. **687**, 595 (2011).

[68]B. Pradenas, I. Araya, M. G. Clerc, C. Falcon, P. Gandhi, and E. Knobloch, Phys. Rev. Fluids **2**, 064401 (2017).

[69]D. Avitabile, D. J. B. Lloyd, J. Burke, E. Knobloch, and B. Sandstede, SIAM J. Appl. Dyn. Syst. **9**, 704 (2010).

[70]D. J. B. Lloyd, B. Sandstede, D. Avitabile, and A. R. Champneys, SIAM J. Appl. Dyn. Syst. **7**, 1049 (2008).

[71]K. R. Elder and M. Grant, Phys. Rev. E **70**, 051605 (2004).

[72]*Numerical Continuation Methods for Dynamical Systems*, edited by B. Krauskopf, H. M. Osinga, and J. Galan-Vioque (Springer, Dordrecht, 2007).

[73]H. A. Dijkstra, F. W. Wubs, A. K. Cliffe, E. Doedel, I. F. Dragomirescu, B. Eckhardt, A. Y. Gelfgat, A. Hazel, V. Lucarini, A. G. Salinger, E. T. Phipps, J. Sanchez-Umbria, H. Schuttelaars, L. S. Tuckerman, and U. Thiele, Commun. Comput. Phys. **15**, 1 (2014).

[74]E. Doedel, H. B. Keller, and J. P. Kernevez, Int. J. Bifurcation Chaos **1**, 493 (1991).

[75]E. J. Doedel and B. E. Oldeman, *AUTO07p: Continuation and Bifurcation Software for Ordinary Differential Equations* (Concordia University, Montreal, 2009).

[76]*Münsteranian Torturials on Nonlinear Science: Continuation*, edited by U. Thiele, O. Kamps, and S. V. Gurevich (CeNoS, Münster, 2014), see http://www.uni-muenster.de/CeNoS/Lehre/Tutorials.

[77]U. Thiele, T. Frohoff-Hülsmann, S. Engelnkemper, E. Knobloch, and A. J. Archer, New J. Phys. **21**, 123021 (2019).

[78]F. Stegemerten, S. V. Gurevich, and U. Thiele, Chaos **30**, 053136 (2020).

[79]S. Trinschek, F. Stegemerten, K. John, and U. Thiele, Phys. Rev. E **101**, 062802 (2020).

[80]A. S. Landsberg and E. Knobloch, Phys. Lett. A **159**, 17 (1991).

[81]M. Suzuki, T. Ohta, M. Mimura, and H. Sakaguchi, Phys. Rev. E **52**, 3645 (1995).

[82]N. Akhmediev, J. M. Soto-Crespo, and G. Town, Phys. Rev. E **63**, 056602 (2001).

[83]W. Barten, M. Lücke, M. Kamps, and R. Schmitz, Phys. Rev. E **51**, 5662 (1995).

[84]T. Watanabe, M. Iima, and Y. Nishiura, J. Fluid Mech. **712**, 219 (2012).

[85]Y. Nishiura, T. Teramoto, and K. I. Ueda, Chaos **13**, 962 (2003).

[86]H. R. Brand and R. J. Deissler, Phys. Rev. Lett. **63**, 2801 (1989).

[87] I. Mercader, O. Batiste, A. Alonso, and E. Knobloch, J. Fluid Mech. **722**, 240 (2013).

[88] Y. Nishiura, T. Teramoto, and K. I. Ueda, Phys. Rev. E **67**, 056210 (2003).

[89] M. Bode, A. W. Liehr, C. P. Schenk, and H.-G. Purwins, Phys. D **161**, 45 (2002).

[90] A. W. Liehr, *Dissipative Solitons in Reaction-Diffusion Systems* (Springer, 2013).

[91] S. M. Houghton and E. Knobloch, Phys. Rev. E **84**, 016204 (2011).

[92] P. Kolodner, Phys. Rev. A **46**, 6452 (1992).

[93] P. Kolodner, Phys. Rev. E **48**, R665 (1993).

[94] T.-S. Lin, S. Rogers, D. Tseluiko, and U. Thiele, Phys. Fluids **28**, 082102 (2016).

[95] W. Tewes, M. Wilczek, S. V. Gurevich, and U. Thiele, Phys. Rev. Fluids **4**, 123903 (2019).

[96] S. Praetorius, A. Voigt, R. Wittkowski, and H. Löwen, Phys. Rev. E **97**, 052615 (2018).

[97] A. Doostmohammadi, T. N. Shendruk, K. Thijssen, and J. M. Yeomans, Nat. Commun. **8**, 1 (2017).

[98] T. Frohoff-Hülsmann, J. Wrembel, and U. Thiele, "Linear and nonlinear suppression of coarsening in nonvariationally coupled Cahn–Hilliard equations," preprint http://arxiv.org/abs/2009.14287 (2020).

[99] Y. Nishiura, T. Teramoto, and K.-I. Ueda, Chaos **15**, 047509 (2005).

[100] A. S. Moskalenko, A. W. Liehr, and H.-G. Purwins, Europhys. Lett. **63**, 361 (2003).

[101] I. Buttinoni, J. Bialké, F. Kümmel, H. Löwen, C. Bechinger, and T. Speck, Phys. Rev. Lett. **110**, 238301 (2013).

[102] L. Ophaus, J. Kirchner, S. V. Gurevich, and U. Thiele, "Data supplement for 'Phase-Field-Crystal description of active crystallites: Elastic and inelastic collisions'," Zenodo. https://www.zenodo.org/record/4322992.